NTNU

Norwegian University of
Science and Technology

Numerical investigation of flow around intersecting cylinders as part of a net structure

Hao Wu

Marine Technology
Submission date: January 2017
Supervisor: Bjørnar Pettersen, IMT
Co-supervisor: Pascal Klebert, SINTEF Fisheries and Aquaculture

Norwegian University of Science and Technology
Department of Marine Technology

NTNU – Trondheim
Norwegian University of
Science and Technology

NUMERICAL INVESTIGATION OF FLOW AROUND INTERSECTING CYLINDERS AS PART OF A NET STRUCTURE.

Hao Wu

January 2017

MASTER THESIS

Department of Marine Technology

Norwegian University of Science and Technology

Supervisor 1: Prof. Bjørnar Pettersen

Supervisor 2: Dr. Pascal Klebert

Supervisor 3: Dr.Tufan Arslan

NTNU
Norwegian University of Science and Technology
Department of Marine Technology

MASTER THESIS IN MARINE HYDRODYNAMICS
FALL 2016

FOR

Stud.techn. Hao Wu

NUMERICAL INVESTIGATION OF FLOW AROUND INTERSECTING CYLINDERS AS PART OF A NET STRUCTURE.

Motivated by the flow through a fish net, either as an isolated net structure or part of a more complex sea farm, the candidate shall investigate the detailed flow around the individual parts of the structure, i.e. circular cylinders in different configurations. The circular cylinders are a simplification of the twins and knots the net is made of. The flow shall be simulated by use of viscous flow simulation tools (CFD), with Ansys-FLUENT.

Through a literature study, the candidate should give an overview of the status of experimental and numerical studies of flow through a net.

Starting from one three-dimensional circular cylinder part, a natural next step will be to study two intersecting cylinders. Several of these may again be parts of a bigger net area.
The candidate must specify all assumptions made about, geometry, computational parameters, boundary conditions and all relevant flow properties, in special turbulence models investigated. In order to expand the basic cross-cylinder-model to more complicated geometries, special attention should be paid to effective grid generation approaches.

Details of the flow field and fluid forces acting on the net must be documented and discussed. Relevant cases to be investigated should be discussed with the supervisors.

General part.
In the thesis, the candidate shall present his personal contribution to the resolution of the problem within the scope of the thesis work. Theories and conclusions should be based on mathematical derivation and logic reasoning identifying the various steps in the deduction. The original contribution of the candidate and material taken from other sources shall be clearly defined. Work from other sources shall be properly referred to. The candidate should utilize the existing possibilities for obtaining relevant literature.
The thesis should be organized in a rational manner to give a clear exposition of results, assessments and conclusions. The text should be brief and to the point, with a clear language.

The thesis shall contain the following elements: A text defining the scope, preface, list of contents, summary, main body of thesis, conclusions with recommendations for further work, list of symbols and acronyms, references and appendices. All figures, tables and equations shall be numerated.
It is supposed that Department of Marine Technology, NTNU, can use the results freely in its research work by referring to the student's thesis. The thesis shall be submitted January 22nd, 2017.

Bjørnar Pettersen
Professor/supervisor

Co-supervisor: Dr Pascal Klebert, SINTEF Fisheries and Aquaculture
Dr Tufan Arslan, ITEA, NTNU

Preface

This is my Master's thesis at Norwegian University of Science and Technology (NTNU) as part of the study program Marine Technology. The project was carried out during the autumn semeter of 2016 in collaboration with the Department of Marine Technology.

I would like to express my gratitude to the following people during this Master's thesis. I would like to thank my supervisor Bjørnar Pettersen for his long-term guidance. I would like to thank Tufan Arslan for answering my questions on the software, and also Pascal Klebert for providing the precious experimental data from SINTEF. A special thanks to NTNU HPC group for the high performance computer Vilje.

Trondheim, 2017-01-15

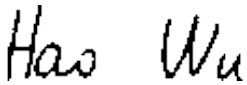

Hao Wu

Abstract

Interference effects occurs in the wake of cylindrical bodies. In marine fishery and aquaculture industry, circular cylinder is very common in offshore fish farm. The cage, as a knot structure, is consist of intersecting ropes. Assuming the deformation on the fish cage is negligible, one can simplify the net into multiple intersecting cylinders. This thesis investigates the flow through a cross-cylinder structure in a numerical method. A RANS approach is applied to accomplish the modeling.

In this thesis, two cases are considered. The first case is a three dimensional modeling of flow around a circular cylinder in a uniform flow. The Reynolds number is 3900, very close to the second case and frequently used in published articles. As a preliminary job, this case investigates the suitable numerical environment for an ambient flow problem including the geometry of domain, grid generation and solver setups. A series of published articles from both experimental and numerical studies are used in comparison to the present simulation. By doing a mesh convergence test, a relatively fine mesh is obtained with the y^+ less than 1 at the first cell layer. Through a parameter analysis, a $k-\omega$ SST turbulence model is selected. The boundary conditions and a suitable time step are also determined. This case gives reasonable results such as velocity and force coefficients after a comparison to the previous work. The CFD model run by ANSYS Fluent is proved to be sufficient for the flow problem with more complicated geometry.

The second case is a cruciform circular cylinder in a uniform flow subjected to Reynolds number 6400. The discussion in the first case gives experience to set up the numerical model. The geometry of domain and structure is based on a PIV model test by Department of Marine Technology at NTNU. Mesh quality is checked by a series of mesh metrics. The characteristics of the fluid flow, such as velocity and pressure, are obtained. In order to validate the model, velocity contours and pressure distribution at different planes are compared with the measurements from corresponding physical model tests. The comparisons show that the numerical results are in an overall agreement with the experimental data. Some interesting phenomenon are also found such as the secondary flow in the spanwise direction.

List of Abbreviations

CFD	Computational Fluid Dynamics
PIV	Particle Image Velocimetry
PDE	Partial Differential Equation
FVM	Finite Volume Method
CV	Control Volume
RANS	Reynolds-Averaged Navier-Stokes equations
DNS	Direct Numerical Simulation
LES	Large Eddy Simulation
RMS	Root Mean Square
SST	Shear Stress Transport
FMG	Full Multigrid
2D	Two-dimensional
3D	Three-dimensional

List of Symbols

A	[m^2]	Projected area on a plane normal to the direction of flow
C_D	[-]	Drag coefficient
$\overline{C_D}$	[-]	Mean drag coefficient
C_L	[-]	Lift coefficient
$C_{L.rms}$	[-]	Root mean square of lift coefficient
C_p	[-]	Pressure coefficient
C_{pb}	[-]	Base pressure coefficient
D	[m]	Diameter of circular cylinder
D_1	[m]	Diameter of single cylinder
D_2	[m]	Diameter of intersecting cylinders
F_D	[N]	Drag force
F_L	[N]	Lift force
f_v	[Hz]	Vortex shedding frequency
h_1	[m]	Thickness of first cell layer for single cylinder case
h_2	[m]	Thickness of first cell layer for intersecting cylinder case
k	[m^2/s^2]	Turbulent kinetic energy
L	[m]	Characteristic length of structure
M	[m]	Spanwise length of intersecting cylinders
p	[Pa]	Pressure
p_{static}	[Pa]	Static pressure
Re	[-]	Reynolds number
Re_{crit}	[-]	Critical Reynolds number
St	[-]	Strouhal number
t	[s]	Time
T	[s]	Period
U_∞	[m/s]	Free stream velocity
u_i	[m/s]	Velocity component
u^*	[m/s]	Shear stress velocity

u^+	[-]	Dimensionless velocity
U_n	[-]	Normalized velocity
$\overline{u_i u_j}$	[m^2/s^2]	Reynolds stress component
y^+	[-]	Dimensionless distance from the wall
δ	[m]	Boundary layer thickness
δ_{ij}	[-]	Kronecker delta
Δt	[s]	Time step
Δx	[m]	Element length in the domain
ρ	[kg/m^3]	Fluid density
τ_w	[Pa]	Surface shear stress
μ	[kg/ms]	Dynamic viscosity of fluid
ν	[m^2/s]	Kinematic viscosity of fluid
ν_T	[m^2/s]	Turbulent viscosity of fluid
ϵ	[m^2/s^3]	Rate of dissipation of turbulent kinetic energy
ω	[m^2/s^3]	Specific rate of dissipation of turbulent kinetic energy
θ	[degree]	Angle of point location on the cylinder

List of Figures

List of Tables

Contents

Chapter 1

Introduction

1.1 Background

Marine fishery and aquaculture is becoming an issue in marine technology nowadays. Offshore fish farm the main tool to raise large quantities of fish. Since such open-ocean structure is very sensitive to the environment, it is very important to understand the fluid characteristics around a fish cage.

The numerical simulation focuses on the fluid structure interaction with turbulence theory. On the one hand, net structures make a shielding effect on the water, and alters the fluid motion through the holes. A popular numerical approach is porous media model, where the fish net is modelled by a thin sheet of porous material. Porosity and pressure drop through the porous zone are defined on the porous media. Patursson et al. (2006) first introduced porous media to fish cage problems. He later acquired current reduction and surface force on a rigid net and reached an overall agreement with his experiment (Patursson et al. (2010)). Many numerical investigations were followed, based on this indirect method. Zhao et al. (2013) simulated the flow inside a gravity cage. Bi et al. (2014) used a flexible porous media model to study the interaction between the flow and structure.

On the other hand, ocean current and wave cause oscillation and hydrodynamic force on the structure. DeCew et al. (2010) modeled the dynamic response of a moored submersible fish cage exposed to current with a modified Morrison Equation. Lader developed a dynamic model for a cylindrical net structure (Lader et al. (2003)) and a net sheet (Lader and Fredheim (2006))

exposed to waves and current. Zhao et al. (2007) investigated the effect of weight system on the hydrodynamic behavior of a gravity cage in current flow.

Experimental research can be full scale test and model test. Full scale test is the direct way. These tests are often carried out at the location of commercial fish farms, where the operation condition is monitored and recorded in the real sea states. Gansel et al. (2014) used dye experiment and recorded how the movement of salmon inside the cage affects the water motion. Lader et al. (2008) documented the net deformation in various current flow conditions at two working Atlantic salmon farms.

Lab test is another approach. The advantage is that it can create the wanted water conditions in low cost. Lader and Enerhaug (2005) measured the forces and deformation on a flexible cage model with different bottom weights under uniform flow. Zhan et al. (2006) tested a submerged net and investigated the effects of Reynolds number, net solidity and flow direction on the drag force. Harendza et al. (2008) tested a inclined cylinder shaped fish cages and recorded the fluid field in front and the wake formation behind the model.

If the ropes on the fish net is assumed sufficiently rigid, one can think that the net structure is consist of many intersecting cylinders. An individual part on the structure, consist of a pair of intersecting cylinders, forms the basic unit. The fluid field behind this basic unit is a new topic in recent years. Only a few experiments were conducted by Osaka et al. (1983), Zdravkovich (1985) and Fox and Toy (1990). They tested single cruciform cylinder and found the fluid region is three-dimensional near wall and more two dimensional away from the junction point on the structure.

The present study investigates the fluid flow passing through a grid structure through a numerical approach. A lab experiment, operated by the Department of Marine Technology at NTNU, is selected as the reference.

The model test was set up in the MC Lab towing tank by using PIV equipments. Figure 1.1 illustrates the experiment environment. The grid structure (white circle in the figure) was fixed in the tank, subjected to a uniform velocity 0.2 m/s. Figure 1.2 is the photo of the grid structure. The fringe of the grid is reinforced by a rectangular frame. The grid has 5 bars both vertically and horizontally. The diameter of each bar is 32mm and spacing between two adjacent bars is 150mm, making it subject to a Reynolds number 6400. Part of results in the experiment is

published by Muthanna et al. (2008).

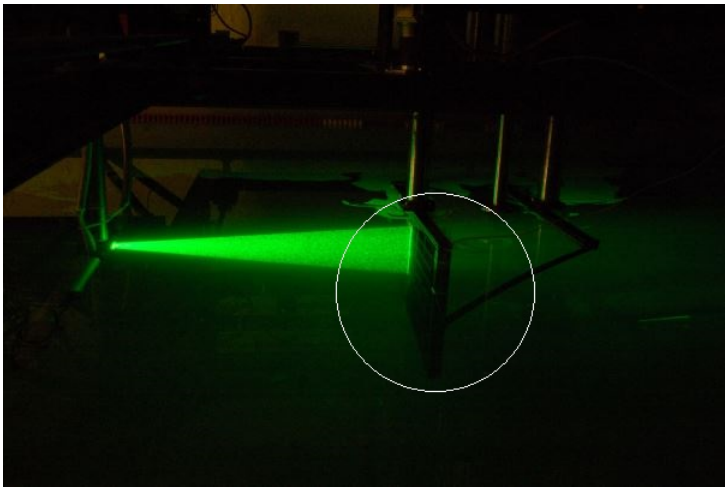

Figure 1.1: Experimental setup in MC Lab.

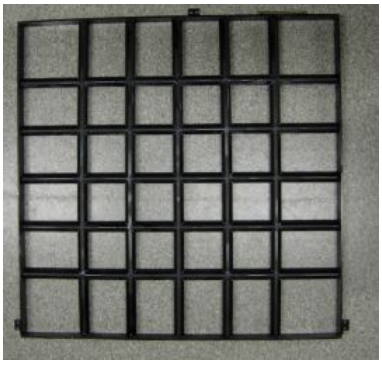

Figure 1.2: Tested grid structure.

1.2 Definition of Problem

The thesis begins with a basic case where three-dimensional flow around a single circular cylinder is simulated. The purpose is to find a suitable computational settings including fluid domain, mesh, turbulence models, and boundary conditions. The Reynolds number is 3900, very close to the experiment so that a number of published articles are available. The main hydrodynamic quantities are then compared to previous articles in order to prove that the current numerical model is capable of a more complex geometry at a similar Reynolds number.

Based on the numerical settings in first case, the second case simulates the flow behind the intersecting cylinders at Reynolds number 6400. The simulation results are validated in a simple comparison to the data in the lab test and other interesting phenomenon is also discussed.

In the second case, the simulation only model one or more basic nodes. Figure 1.3 explains the division of the structure. The basic node unit is surrounded by the dashed line. Each unit has the same size with its neighbour unit. The unit has a spanwise length equal to M=0.15 m and a diameter D=0.032 m.

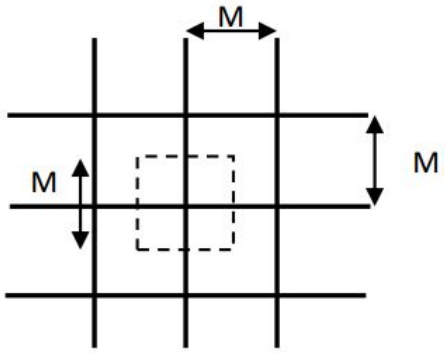

Figure 1.3: The division of the structure.

1.3 Structure of the Report

- Chapter 2 gives a review to theoretical background of fluid mechanics. It describes in details typical fluid phenomenons for circular cylinder, turbulence and government equations.
- Chapter 3 explains the concept of CFD and its main procedures, in terms of mesh methods, turbulence models, interpolation, discretization, and numerical solvers. A commercial CFD tool, ANSYS, is also introduced.
- Chapter 4 introduces the complete pre-processing work in the software. Each procedure is explained in details.
- Chapter 5 presents the main results for the two cases: single cylinder and intersecting cylinders, and provide detailed discussion related to the results.

- Chapter 6 gives the main conclusion of two cases.
- Chapter 7 gives brief recommendations for further work.

Chapter 2

Theoretical Background

This chapter gives an review of basic theory in the analysis of flow around a submerged cylindrical structure. The flow characteristics for turbulence is explained.

2.1 Fluid property

When a flow with uniform velocity is attached to a cylinder in the cross section profile, a velocity gradient generates at the body surface. The velocity decreases to zero towards the surface within a vertical distance. The distance is called boundary layer, with a thickness known as δ. The boundary layer develops along the body surface, pressure gradient gradually reduces below zero, and flow separation takes place.

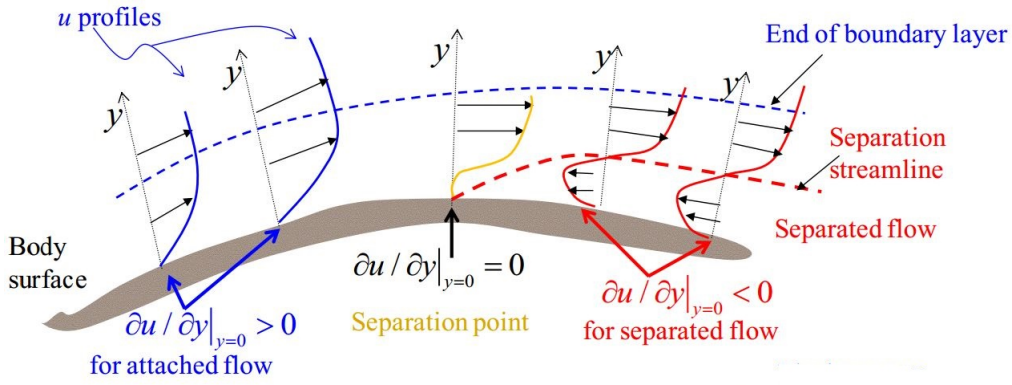

Figure 2.1: Development of a laminar boundary layer.

A very important non-dimensional parameter to describe the fluid property is Reynolds

number Re, its general definition is

$$Re = \frac{\rho U L}{\mu} \tag{2.1}$$

where ρ is the fluid density, U is the characteristic velocity, L is the characteristic length, μ is the dynamic viscosity.

In present work, the characteristic length is the diameter D. Hence the Reynolds number is defined as

$$Re_D = \frac{\rho U D}{\mu} \tag{2.2}$$

Theory about smooth circular cylinder was established by Sumer and Fredsøe (1997). According to the value of Re_D, the flow regimes are distinguished.

At very small value of Re_D, the flow separation does not happen on the body surface and the flow is known as creeping flow. The surface flow starts to separate and the wake remains symmetric when Re_D>5. For 40<Re_D<150, the wake becomes unstable and Karman vortex street appears in the wake, where the vortices are shed alternatively from the two separation points. As the Reynolds number continues growing up, the flow becomes three dimensional due to instability. For this flow regime when Re_D<2×10^5, turbulence occurs in shear layer and separation point moves downstream side of the cylinder, but the boundary layer on the body surface is still laminar before separation. This flow regime is named subcritical flow regime.

For 2×10^5<Re_D<5×10^5, the boundary layer experiences a transition from laminar to turbulent. This flow regime is called critical flow regime.

For 5×10^5<Re_D<3×10^6, the transition to turbulence continues and takes place between stagnation point and separation point. This flow regime is called supercritical flow regime.

For larger Reynolds number when Re_D>3×10^6, the boundary layer becomes fully turbulent. This flow regime is called transcritical flow regime.

This thesis studies a single cylinder case at Re_D=3900, at the subcritical flow regime. For intersecting cylinders, the flow regime may differ due to the interference effects.

2.2 Mass Conservation and Momentum Conservation

Generally, the equations that describe the flow in the fluid domain are the continuity equation and momentum conservation equation.

Continuity equation states that in a fluid element, the rate of change of mass flow is equal to the rate of mass flow into the same element. For incompressible fluid, the continuity equation can be written as:

$$\frac{\partial u}{\partial x}+\frac{\partial v}{\partial y}+\frac{\partial w}{\partial z}=0 \tag{2.3}$$

where u, v, w represents the velocity fluid.

Momentum conservation equation states that the rate of change of momentum for a fluid particle is equal to the sum of forces on it. For Newtonian fluid, where viscous stress is linearly proportional to the local strain rate, momentum conservation equation is called Navier-Stokes equations. Navier-Stokes equations for incompressible fluid are shown below:

$$\frac{\partial u}{\partial t}+(\vec{u}\cdot\bigtriangledown)u=-\frac{1}{\rho}\frac{\partial p}{\partial x}+\nu(\bigtriangledown^2\cdot u) \tag{2.4}$$

$$\frac{\partial v}{\partial t}+(\vec{u}\cdot\bigtriangledown)v=-\frac{1}{\rho}\frac{\partial p}{\partial y}+\nu(\bigtriangledown^2\cdot v) \tag{2.5}$$

$$\frac{\partial w}{\partial t}+(\vec{u}\cdot\bigtriangledown)w=-\frac{1}{\rho}\frac{\partial p}{\partial z}+\nu(\bigtriangledown^2\cdot w) \tag{2.6}$$

where $\vec{u}$ represents the velocity vector with three velocity components u, v, w. p represents pressure. ν represents kinematic viscosity.

2.3 Force on the body

The vertex shedding in the wake always causes two oscillating force components: a force F_L normal to the inflow direction, and a force F_D in the flow direction, known as lift force and drag force.

The non-dimensional expression for lift and drag force are known as lift coefficient and drag coefficient, shown as

$$C_L = \frac{F_L}{\frac{1}{2}\rho U_\infty^2 A} \tag{2.7}$$

$$C_D = \frac{F_D}{\frac{1}{2}\rho U_\infty^2 A} \tag{2.8}$$

where A is the projected area normal to the flow direction.

Drag coefficient is usually evaluated by its mean value $\overline{C_D}$. Figure 2.2 shows how time average drag coefficient varies at different Reynolds numbers.

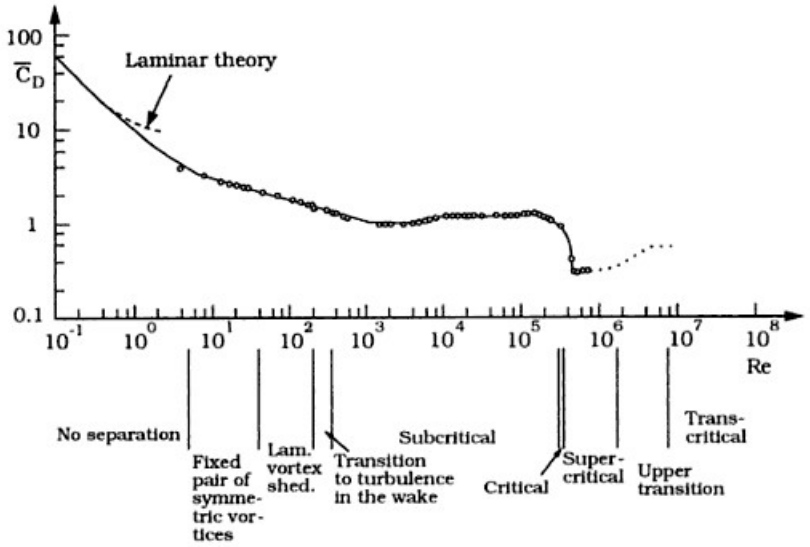

Figure 2.2: Drag coefficient (Sumer and Fredsøe (1997)).

A root mean square (RMS) value is introduced to evaluate the lift force, defined as

$$C_{L,rms} = \sqrt{\overline{C_{L'}^2}} \tag{2.9}$$

where $C_{L'}$ is the distance to the maximum value for C_L in each shedding period.

The lift force oscillates with the vortex shedding frequency f_v, while the drag force oscillates with twice of that frequency. The vortex shedding frequency f_v is often represented by a non-dimensional coefficient called Strouhal number, which is defined as:

$$St = \frac{D f_v}{U_\infty} \tag{2.10}$$

Figure 2.3 shows the Strouhal number at different Reynolds numbers.

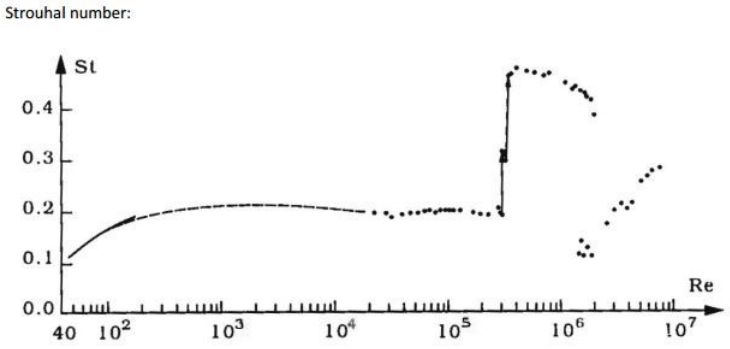

Figure 2.3: Strouhal number (Sumer and Fredsøe (1997)).

Similarly, the non-dimensional pressure along the body is

$$C_p = \frac{p - p_\infty}{\frac{1}{2}\rho U_\infty^2} \tag{2.11}$$

where p_∞ is the free stream static pressure.

The values of C_p at different locations θ on the body surface is of interest. Therefore C_p is usually plotted as a function of θ along the perimeter of the cylinder.

Base pressure coefficient C_{pb} is another important variable to describe pressure distribution. It reflects the pressure behind the separation point on the structure. For single circular cylinder, flow separation is of little difference across the span so C_{pb} is a constant value at different spanwise places. For intersecting cylinders, the interference effects result in the variation along the span, and the variation of C_{pb} is studied.

2.4 Turbulence

There are two flow conditions called laminar flow and turbulence flow. When the flow velocity is larger than a critical Reynolds number Re_{crit}, the fluid flow is turbulent.

In turbulence, all the fluid variables vary randomly both in space and in time, involving velocity, pressure, vorticity and temperature. From a Reynolds approach, the variables are characterized by decomposition. As an example, Figure 2.4 illustrates the time history of velocity component and the decomposition based on Reynolds assumption.

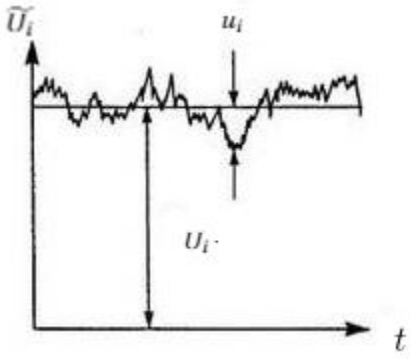

Figure 2.4: Time history of velocity component.

In Figure 2.4, the instantaneous velocity component $\widetilde{U_i}$ is decomposed into a mean value U_i and small fluctuation u_i. Reynolds decomposition for velocity is given below:

$$\widetilde{U_i} = U_i + u_i \tag{2.12}$$

The mean part U_i is the time averaged description of the instantaneous velocity. u_i is a small disturbance fluctuating around the mean value. The fluctuation is always three-dimensional even in two-dimensional flow.

The turbulence tends to occur in a boundary layer. Figure 2.5 shows the typical transition from laminar flow to turbulence at the edge of a flat plate. Initially, a laminar boundary layer develops due to the no-slip condition at the wall. After some distance, the small chaotic oscillation arises and disturbs the flow and the boundary layer flow becomes turbulent.

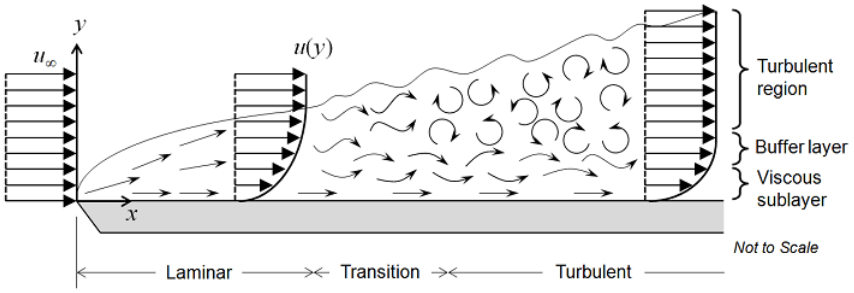

Figure 2.5: Transition to turbulence for a flat plate.

In the turbulent boundary layer, both viscosity and turbulence act on the flow characteristics. The performance of fluid varies as the distance from wall changes. Considering viscous and

turbulent effect, non-dimensional variables are introduced to describe the fluid characteristics in the turbulent boundary layer, which are velocity u^+ and distance from the wall y^+

$$u^+ = \frac{U}{u*} \tag{2.13}$$

$$y^+ = \frac{yu*}{\nu} \tag{2.14}$$

where $u* = \sqrt{\frac{\tau_w}{\rho}}$ is the skin friction velocity, τ_w is the surface shear stress, y is the distance from the wall.

u^+ is a function y^+, and the relationship is then established as

$$u^+ = f(y^+) \tag{2.15}$$

As shown in Figure 2.5, a fully developed turbulent boundary layer can be further divided into three parts.

At the very thin distance away from the wall (y^+<5), turbulence effect remains very small and velocity is linear with the distance from the wall. This is called viscous sublayer or linear sublayer. The law is given as

$$u^+ = y^+ \tag{2.16}$$

Above the viscous sublayer, the layer is called buffer layer. In buffer layer, turbulence begins to influence the velocity and causes a flow transition to turbulence. No exact expression is satisfied in this transition layer.

When the flow continues being away from the wall (y^+>30), the transition is completely finished and there is no viscous effect. In this layer the flow velocity satisfies a logarithmic law and thereby is named log-law region.

$$u^+ = \frac{1}{\kappa} ln(y^+) + A \tag{2.17}$$

where the parameters κ=0.4, A=5.

Figure 2.6 gives the complete law of the wall in the turbulent boundary layer. The velocity

first increase linearly in viscous sublayer, then goes through a transition in buffer layer, and finally yields a log law. In turbulence theory, the entire turbulent boundary layer is not always resolved. Sometimes researcher only concerns log law layer and therefore requires y^+>30 at first cell layer.

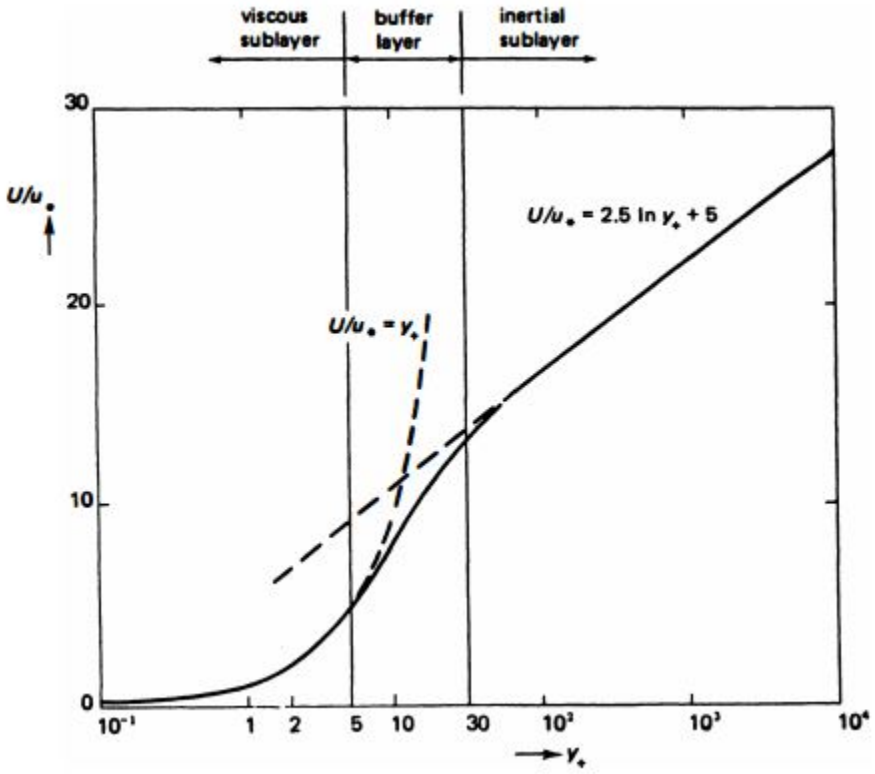

Figure 2.6: The law of the wall. (Tennekes and Lumley (1972))

Chapter 3

Computational Fluid Dynamics

This chapter introduces the concept of CFD and gives a description of how CFD works for the entire process.

3.1 Introduction to CFD

Fluid flow is commonly studied in three ways: experimental, theoretical or numerical method. Motivated by the aerospace industry in the 20th century, a new numerical approach, called Computational Fluid Dynamics, has been developing with the assistance of mathematical theory, grid generation technology and computer science.

Figure 3.1 illustrates how CFD works in a regular path. Firstly, the geometries of the structure and fluid domain are defined to fit the following calculation. The fluid domain is then discretized into a number of grids. The governing equations are solved in each grid, which is also referred to element or cell. Usually finer mesh provides more accurate results but also needs increasing computational cost. Flow solver and boundary conditions are specified according to the fluid property as the last step in the pre-processing stage. After computing, the results are judged and only the results in good quality are visualized in the post processing.

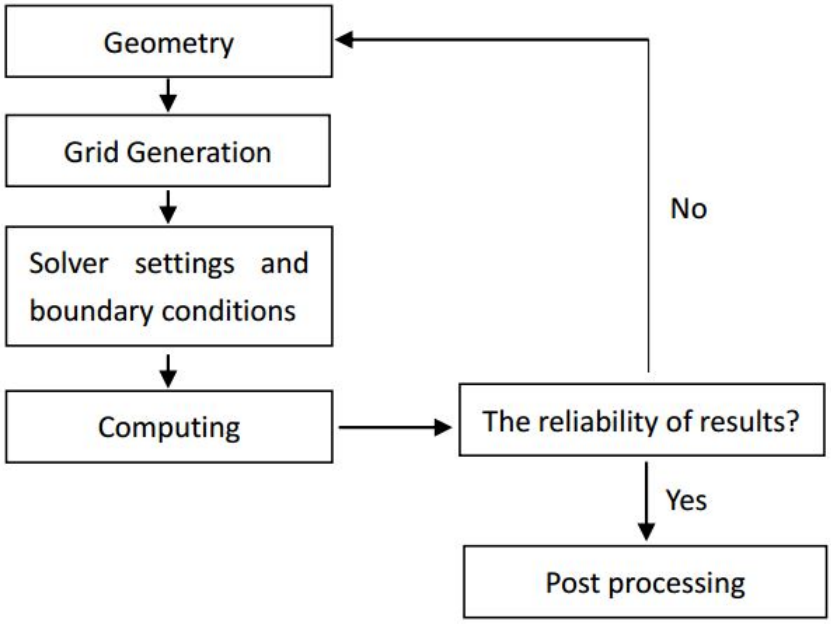

Figure 3.1: Flow chart for a typical CFD.

3.2 Mesh

In general, analytical solutions of velocity, pressure are not available. Therefore, the fluid domain is divided into small mesh cells. For three-dimensional cases, these small cells are made up of enclosed volumes in various shapes, for instance, hexahedra and tetrahedra. The governing equations are resolved after discretization, and numerical solutions of flow variables (velocity, temperature) are calculated and stored in each mesh cell.

mesh can be simply classified into two types: structured grid and unstructured grid. Figure 3.2 gives an example of unstructured and structured mesh for two-dimensional case. For structured mesh, each element can be numbered by two indices i and j as shown in Figure 3.2. For instance, the node in the circle can be represented by $i5\,j4$. Unlike structured mesh, each node in unstructured mesh cannot be located by a pair of indices.

The main advantage of a structured mesh is that less cells are needed than unstructured mesh and therefore reduces the computational cost. The high quality of mesh enables the results more reliable and easily converged. But structured mesh also results in much workload during meshing. For a geometry with very complex shape, a multi-block grid strategy is applicable where the two types of grids are combined. One of these two grids is specific within each

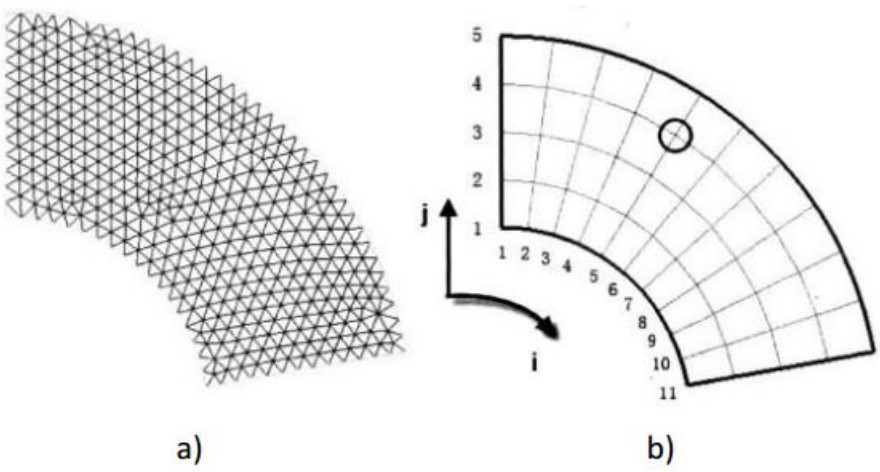

Figure 3.2: Two types of grids: a) Unstructured mesh; b) Structured mesh.

block.

Different physics and solvers have different requirements for mesh quality. The quality of mesh depends on various criteria. ANSYS provides several mesh metrics (ANSYS (2015)). Here three metrics are considered:

- Aspect Ratio
- Skewness
- Orthogonal Quality

Aspect ratio is the ratio between the longest edge and the shortest edge in an element. Ideally, this ratio should be one for all the elements. ANSYS allows an aspect ratio as large as 100. When the flow is multi-dimensional, it is beneficial to keep the ratio small. Skewness is based on the deviation of the inner angle of the element from being 90^o. Orthogonality is based on how close the angles between adjacent element edges, or adjacent element faces, are to the optimal angle 90^o. Orthogonality and skewness has a strong connection.

Table 3.1 and Table 3.2 illustrate quality criteria in terms of skewness and orthogonal quality. Both are defined as a spectrum in a range from 0 to 1. Smaller skewness value but larger orthogonal value mean good mesh quality.

Table 3.1: Skewness mesh metrics spectrum.

Excellent	Very good	Good	Acceptable	Bad	Unacceptable
0-0.25	0.25-0.5	0.5-0.8	0.8-0.94	0.95-0.97	0.98-1

Table 3.2: Orthogonal quality mesh metrics spectrum.

Unacceptable	Bad	Acceptable	Good	Very good	Excellent
0-0.001	0.001-0.14	0.15-0.2	0.2-0.69	0.7-0.95	0.95-1

In addition to the criteria above, the change of size between neighboring elements is also important. The size transition should be smooth. The growth rate of adjacent elements should keep a growth rate typically less than 1.2 (ANSYS (2015)).

3.3 Discretization

Mesh makes it possible to obtain fluid data (velocity, pressure) within each small element. Finite volume method (FVM) is one of the main numerical techniques to solve the data. FVM is used in many commercial CFD solvers, such as Fluent and CFX.

In FVM, a small element is called control volume (CV), and the conservation equations here are named transport equations. The transport equation is an equation of a general scalar quantity ϕ. If ϕ is given specific physical meanings, such as ϕ=1 or ϕ=u_i, the transport equation then corresponds to Equation (2.3), (2.4), (2.5) and (2.6).

The general form of a transport equation can be written as

$$\frac{\partial(\rho\phi)}{\partial t} + \mathrm{div}(\rho\phi\boldsymbol{v}\cdot) = \mathrm{div}(\Gamma \mathrm{grad}\phi) + q_\phi \tag{3.1}$$

where Γ represents diffusion coefficient. q_ϕ represents source or sink of ϕ. This equation contains rate of change term and convective term on the left side, whereas diffusion term and source term lie on the right side.

Finite volume method uses the integral form of the transport equation, which gives the following expression:

$$\frac{\partial}{\partial t}\int_\Omega \rho\phi \mathrm{d}V + \int_S \rho\phi\boldsymbol{v}\cdot\boldsymbol{n}\mathrm{d}S = \int_S \Gamma \mathrm{grad}\phi\cdot\boldsymbol{n}\mathrm{d}S + \int_\Omega q_\phi \mathrm{d}\Omega \tag{3.2}$$

where the volume and total surface of the CV are $d\Omega$ and dS respectively.

To obtain solution in each control volume, a discretization type of transport equation is needed. Figure 3.3 shows a cube control volume.

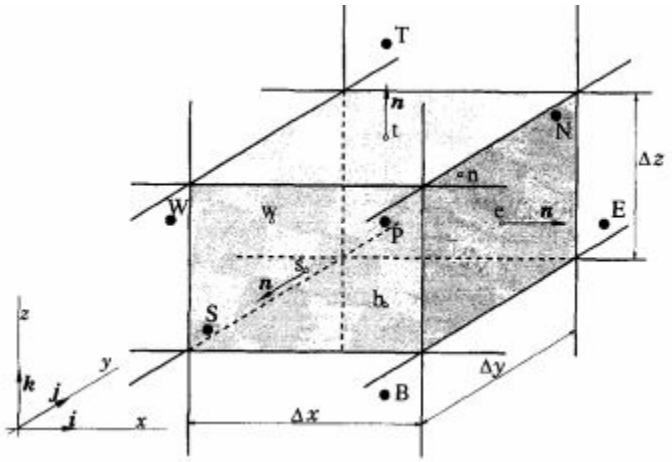

Figure 3.3: A cube control volume and the notation used for a Cartesian 3D grid (Ferziger (2002)).

A computational node (P) is assigned to the center of CV, where the fluid data ϕ_P is calculated and stored. The approximations to the integrals require the values of variables at the six faces other than computational nodes. The face values are firstly expressed by the interpolation of nodal values, and helps abtain ϕ_P in each control volume. Main approaches for interpolation are upwind scheme, linear scheme and higher order scheme.

3.4 Turbulence model

Analytical solution to the original NS equations is impractical for turbulence flow due to its complex behaviors. The numerical approaches can be summarized as Direct Numerical Simulation (DNS), Large Eddy Simulation (LES) and Reynolds average Navier-Stokes equation (RANS).

DNS is the numerical method without modeling. The mesh quality for DNS is sufficiently fine so that even the smallest eddy is captured. The large number of fine mesh cells provides accurate results and is associated with increasing computational cost, therefore DNS is not practical for industrial flows today.

LES makes use of a filtered Navier Stokes equations and only resolves the eddies in larger size. Although its requirement is not as high as DNS, the efforts and computational resources

needed are still too large for complex flow condition.

RANS modifies the original N-S equations through averaging the variables in time, where all the turbulent motion is modeled. This is the most widely used approach for industry. RANS is used in the present work.

RANS is the time averaged version of Navier Stokes equations. It makes use of the Reynolds approach. For velocity $\widetilde{U}$, its mean value U and fluctuation u are given the following assumptions

$$\overline{U} = U, \overline{u} = 0 \tag{3.3}$$

Consequently, mass and momentum conservation are expressed as RANS equations in a tensorial form

$$\frac{\partial U_i}{\partial x_i} = 0 \tag{3.4}$$

$$\frac{\partial U_i}{\partial t} + U_j \frac{\partial U_i}{\partial x_j} = -\frac{1}{\rho}\frac{\partial P}{\partial x_i} + 2\nu \frac{\partial S_{ij}}{\partial x_j} - \frac{\partial \overline{u_i u_j}}{\partial x_j} \tag{3.5}$$

where i, j are tensor indices. $S_{ij} = \frac{1}{2}(\frac{\partial U_i}{\partial x_j} + \frac{\partial U_j}{\partial x_i})$

RANS equations intend to solve all the mean values. However, a new unknown terms Reynolds stress $\overline{u_i u_j}$ is introduced. Due to the presence of Reynolds stress, a turbulent-viscosity hypothesis (Boussinesq (1877)) is introduced to close the equations, which is given as

$$-\overline{u_i u_j} = 2\nu_T S_{ij} - \frac{2}{3} k \delta_{ij} \tag{3.6}$$

where k represents mean turbulence kinetic energy. ν_T represents a generalized eddy viscosity in order to display turbulent effect.

To solve new variables k and ν_T, specific turbulent models are added. During the last decades, more than 100 models were proposed. Based on the number of additional PDEs, turbulent models can be categorized as zero-equation model, one-equation model, two-equation model, seven-equation model.

Two advanced two-equation models are considered in present work: $k-\epsilon$ Realizable model

and $k-\omega$ SST model.

The k-ϵ model is a widely used turbulence model. Realizable k-ϵ model modifies the formulation for turbulent viscosity so as to be more consistent with the physics of turbulent flows. In contrast to traditional k-ϵ model, the ability to predict large pressure gradient is improved with the new formulation (Shih et al. (1995)).

Two additional equations involves turbulent kinetic energy k and dissipation rate ϵ:

$$\frac{\partial(\rho k)}{\partial t}+\frac{\partial(\rho k u_j)}{\partial x_j}=\frac{\partial}{\partial x_j}[(\mu+\frac{\mu_t}{\sigma_k})\frac{\partial k}{\partial x_j}]+G_k+G_b-\rho\epsilon-Y_M+S_k \tag{3.7}$$

$$\frac{\partial(\rho\epsilon)}{\partial t}+\frac{\partial(\rho\epsilon u_j)}{\partial x_j}=\frac{\partial}{\partial x_j}[(\mu+\frac{\mu_t}{\sigma_\epsilon})\frac{\partial\epsilon}{\partial x_j}]+\rho C_1 S\epsilon-\rho C_2\frac{\epsilon^2}{k+\sqrt{\nu\epsilon}}+C_{1\epsilon}\frac{\epsilon}{k}C_{3\epsilon}G_b+S_\epsilon \tag{3.8}$$

where C_1=max[0.43, $\frac{\eta}{\eta+5}$], η=$S\frac{k}{\epsilon}$, $S=\sqrt{2S_{ij}S_{ij}}$. The new terms in the equations are defined in ANSYS (2015).

k-ω SST model is a two-equation eddy viscosity model. The use of a specific dissipation rate ω makes it possible to solve the entire boundary layer including viscous sublayer and can be used as a low-Re turbulence model without any extra damping function (Menter (1993)). k-ω SST model is capable of simulating adverse pressure gradient and flow separation.

The specific dissipation rate ω is defined as

$$\nu_T=\frac{a_1 k}{\max(a_1\omega, SF_2)} \tag{3.9}$$

The additional equations for k and ω are

$$\frac{\partial k}{\partial t}+U_j\frac{\partial k}{\partial x_j}=P_k-\beta^* k\omega+\frac{\partial}{\partial x_j}[(\nu+\sigma_k\nu_T)\frac{\partial k}{\partial x_j}] \tag{3.10}$$

$$\frac{\partial\omega}{\partial t}+U_j\frac{\partial\omega}{\partial x_j}=\alpha S^2-\beta\omega^2+\frac{\partial}{\partial x_j}[(\nu+\sigma_\omega\nu_T)\frac{\partial\omega}{\partial x_j}]+2(1-F_1)\sigma_{\omega^2}\frac{1}{\omega}\frac{\partial k}{\partial x_i}\frac{\partial\omega}{\partial x_i} \tag{3.11}$$

where the new terms represent closure Coefficients and can be found in ANSYS (2015).

When a turbulent model is applied, near wall region is very special. At very high Re, the flow in the boundary layer is complicated, so it is not wise to always perform an accurate solution for all the layers. The resolution in the boundary layer will depend on the simulation requirement.

In general, a wall function is applied and log-law region (y^+>30) is resolved.

In present work, no wall function is performed. This is achieved by defining y^+ less than one at the first cell layer. An enhanced wall treatment is emphasized.

Enhanced wall treatment is a near-wall modeling method that combines a two-layer model. The wall function is called an enhanced wall function. If the near-wall mesh is fine enough to be able to resolve the viscous sublayer ($y^+ \approx 1$ at the first near-wall), then the enhanced wall treatment will be identical to the boundary layer. The restriction for this treatment is that the near-wall mesh must be sufficiently fine everywhere, and leads to large computational requirement.

To achieve the goal of having a near-wall modeling approach that will possess the accuracy of the standard two-layer approach for fine near-wall meshes and that, at the same time, will not significantly reduce accuracy for wall-function meshes, ANSYS Fluent can combine the two-layer model with enhanced wall functions (ANSYS (2015)).

Figure 3.4 gives a simple illustration for standard and enhanced wall treatment. A velocity profile in the boundary layer is expressed by two mesh types. In the left figure, the mesh is very coarse, so the buffer sublayer and viscous layer are involved in the first layer. The figure in the right side, places more cell layers, so even the viscous layer is resolved.

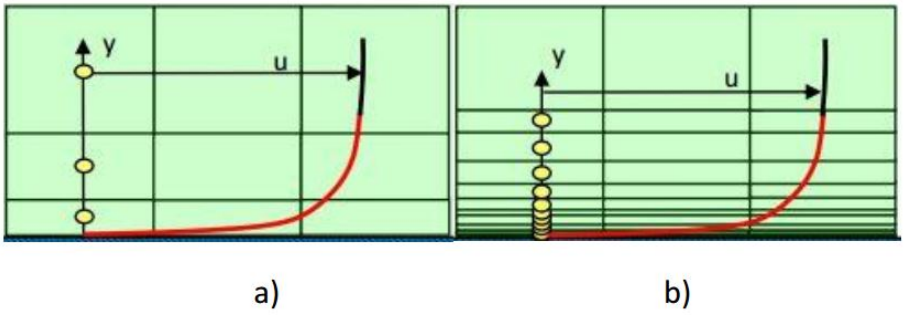

Figure 3.4: Mesh resolution near the wall for the same case: a) logarithmic-based Wall functions b) viscous sublayer resolving approach.

3.5 Courant-Friedrichs-Lewy number

During the whole process, to evaluate the results is an important step that may influence the credibility of the numerical simulation, thus good criterion are necessary.

For unsteady problem, time integration is performed during the simulation. Therefore time step always plays a crucial role to preserve the stability of calculation. The time step in the simulation has a maximum limit where the solved discretized equations will lose its stability and result in significant numerical error. A Courant-Friedrichs-Lewy (CFL) number is referred as the indicator of time step and evaluated within each element. For the present study, an explicit method is applied and thereby the maximum CFL number in the simulation should be kept lower than one (Ferziger (2002)). A suitable CFL number is an important prerequisites for convincing numerical results, and this is realized by changing the time step in the pre processing.

In one dimension, the Courant-Friedrichs-Lewy (CFL) number can defined as

$$CFL = \frac{u\Delta t}{\Delta x} \tag{3.12}$$

where Δt represents time step, u and Δx are the stream wise velocity and element length along the stream wise direction.

For three dimensional problem, the definition is

$$CFL = \sum_{i=1}^{3} \frac{u_i \Delta t}{\Delta x_i} \tag{3.13}$$

where i=1,2,3 represents the three directions.

3.6 ANSYS

ANSYS 16.2 is applied to peform the simulation. ANSYS is a commercial software package and offers a number of engineering applications covering modelling, meshing, solving and post-processing. All the applications necessary for present work is managed in ANSYS Workbench 16.2, a project-management tool. ANSYS Workbench is an interface that links all the individual applications and handles the passing of data between each other (ANSYS (2015)).

Figure 3.5 illustrates the components for the CFD work. The simulation contains three modules. Geometry is used to build up the geometry for structure and the computational domain. Mesh is used to divide the blocks and draw the mesh. The data is then imported into Fluent and used for calculation. Fluent defines the fluid properties, turbulence model, boundary conditions, solver and initial conditions. Residuals and force coefficients are calculated and recorded during the simulation. Fluent is also used for visualization of the results.

Figure 3.5: Setup in ANSYS Workbench.

Chapter 4

Ansys Setup

This chapter explains in detail the pre-processing work of the simulation. Two cases, single cylinder and intersecting cylinders are discussed from geometry making, meshing to solver set-up. The manipulation is associated with ANSYS Workbench.

4.1 Physical parameters

Table 4.1 gives information of initial velocity U, diameter D, density ρ, dynamic viscosity μ and Reynolds number Re.

Table 4.1: Physical parameters.

	U [m/s]	D [m]	ρ [kg/m^3]	μ [kg/ms]	Re [-]
Case 1: single cylinder	$U_1 = 0.122$	0.032	1	10^{-6}	3900
Case 2: intersecting cylinders	$U_2 = 0.20$	0.032	1	10^{-6}	6400

4.2 Domain

A computational domain is defined for the CFD problem and the size of the domain has an influence on the accuracy of result and the cost of computational resources. If the domain is not sufficiently large, the flow may fail to fully develop at the boundary and thus cause the abnormal value of hydrodynamic quantities C_D and C_L on the surface of structure. Conversely, a huge

domain size is also of little significance and impractical due to the limitation of computational time.

Generally, there are two approaches to choose a reasonable domain size. The first approach is through a domain size convergence test. The second one is by referred to the size in similar simulation problem. In present study, the basic strategy is to determine the domain size in retrospect of several former literature studies.

4.2.1 Single cylinder

The case about an infinitely long cylinder has been tested many times for the past. The selection of domain is always considered with the characteristic length of the cylinder.

Box-shaped domain is frequently used for this problem. Palkin et al. used a domain size (X, Y, Z) $25D \times 10D \times 4D$. Franke and Frank (2002) used a domain size (X, Y, Z) $30D \times 20D \times \pi D$. Li (2011) used a domain size (X, Y, Z) $27D \times 9D \times 2.3D$.

In the present study, the shape and size of the domain are illustrated in Figure 4.1. The Cartesian Coordinate system locates at the center of the cylinder. The mainstream U_1 flows in front of the cylinder along a positive X_1 direction. the span of the cylinder is in the Y_1 direction.

The length of domain from the cylinder center to inlet and outlet are $6D$ and $28D$. The distance between top and bottom boundaries are $9D$. The extent of span is πD.

4.2.2 Intersecting cylinders

Figure 4.2 illustrates structure in the domain. The Cartesian Coordinate system locates at the point where the centerline of two cylindrical components intersect. The mainstream U_2 is along X_2 direction.

To simulate the lab environment of the test, the size of domain keeps consistent with the experimental settings. To make the domain match the experiment, the distance from the structure to inlet and outlet are respectively $6D$ and $16D$. The length of the cylinder is equal to the spacing length M.

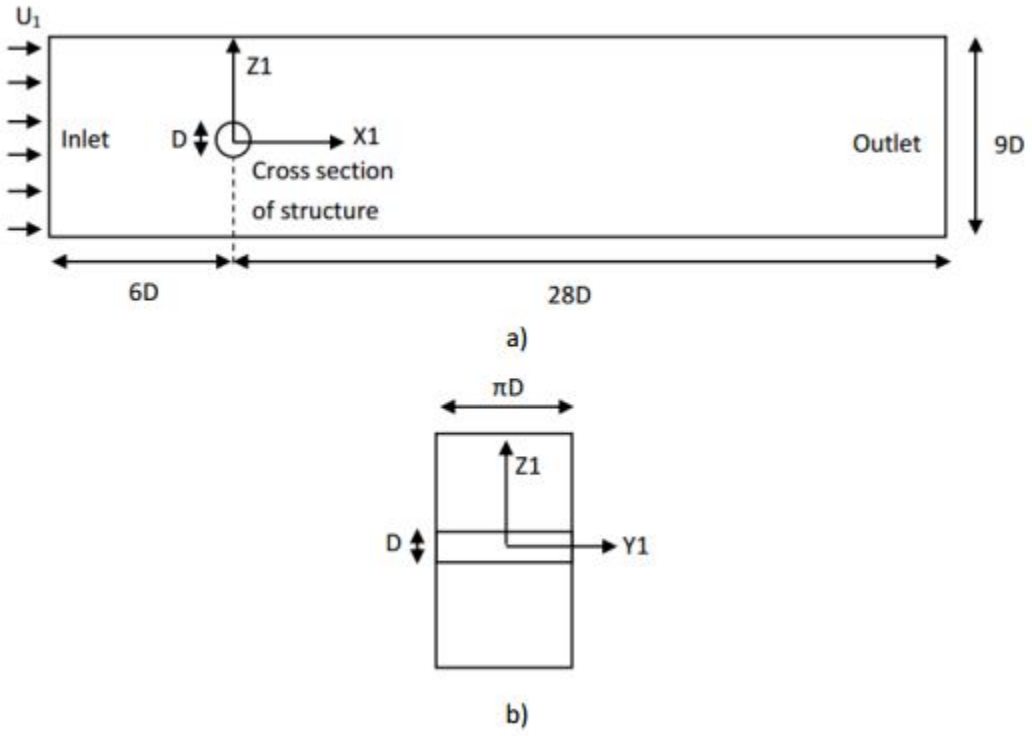

Figure 4.1: Fluid domain for single cylinder: a) side view; b) front view.

4.3 Mesh setup

This study has two different fluid domains for single cylinder and intersecting cylinders. The presence of the structure makes it difficult to provide a structured mesh in equal size. Additionally, to make use of fine mesh every place is a waste of computing resource, such as the upstream and far-away downstream. Hence the mesh setup uses multiple blocks and define specific mesh properties in each block.

4.3.1 Single cylinder

Flow around single cylinder is a frequently studied topic. Mesh strategy for this case has been mature after being tested for many times.

In present study, the domain is meshed by using a similar method by Kravchenko and Moin (2000). This method is proved to be successfully perform the fluid analysis for single cylinder.

For the spanwise direction of the cylinder, the domain is simply equally divided. Actually, this case applies a two-dimensional mesh strategy and simply extruded along the span direc-

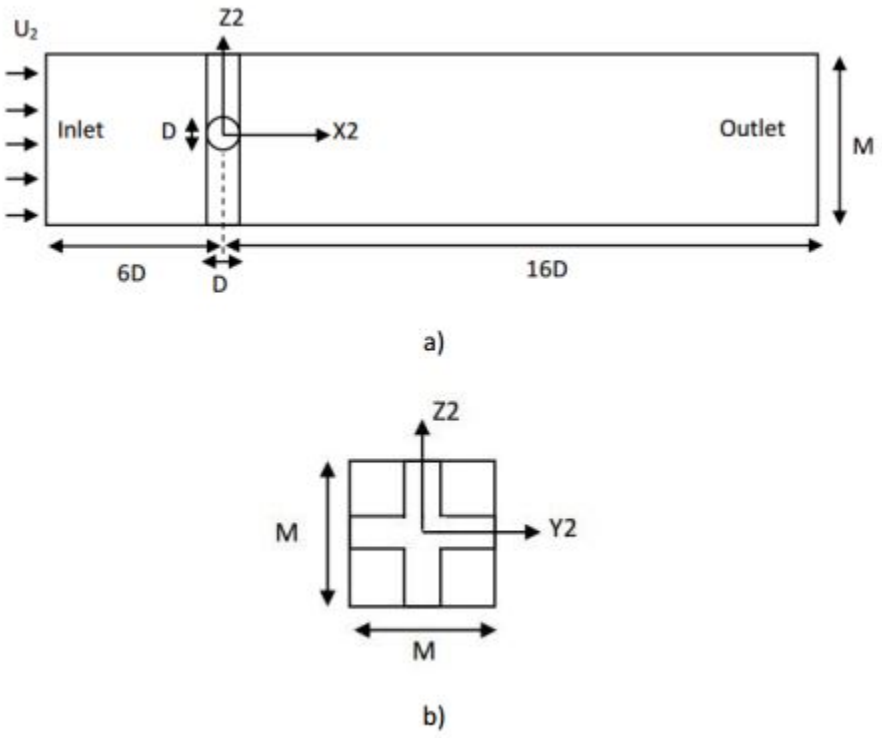

Figure 4.2: Fluid domain for intersecting cylinders: a) side view; b) front view.

tion. The block-typology used for single cylinder is illustrated in Figure 4.3. The blue lines in the figure divides the whole domain into 12 blocks, where the number of cells and growth rate are defined along the block edge. The core region is a hollow square that contains four blocks. The length of the core region is $3D$. The rest rectangular blocks form a far-away region. Compatibility is assured at the edge between adjacent blocks.

The mesh begins in the core region. A large number of points is firstly created along the body surface and then radiated outwards. The number of the division should be sufficiently large because an enhanced wall treatment requires the element size in the first layer near wall. To reduce the computational cost, the far-away region keeps larger cell size than the core region.

The local mesh in the core region is shown in Figure 4.4. The enhanced wall treatment requires the first cell layer at the body surface with its thickness h_1 satisfying a y^+ less than unity so that fluid motion in the viscous sublayer can be captured theoretically. For the first cell layer here, the y^+ value is around 0.9 by limiting the axial length. The size of elements in each layer is the same along the circle. The first layer element is shorter axially with the aspect ratio around

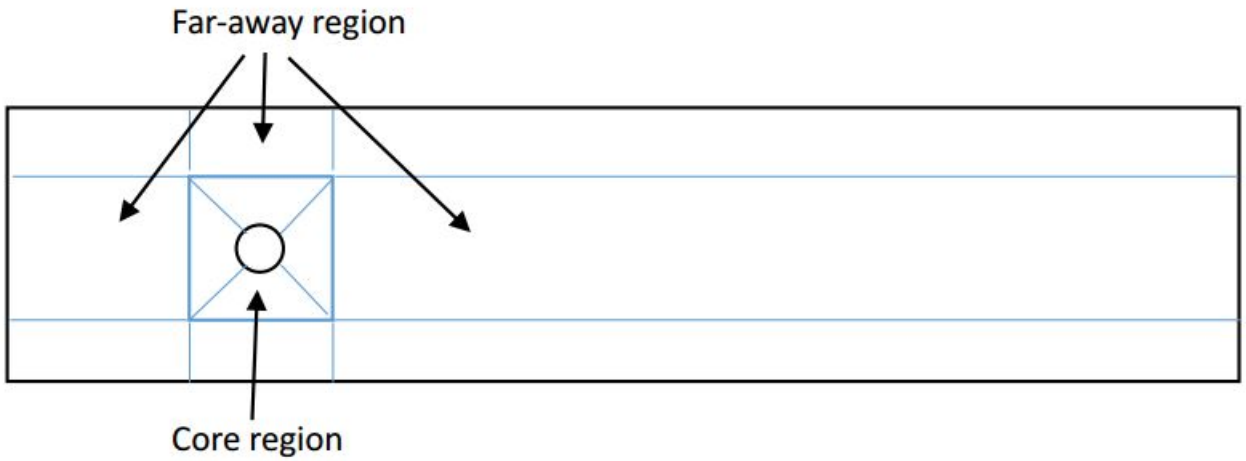

Figure 4.3: The block-typology for single cylinder in side view.

5. To reduce the computational cost, a growth rate is defined along the path outwards. The growth rate is 1.2. In the core region, the edge size grows up as the element moves away from the cylinder.

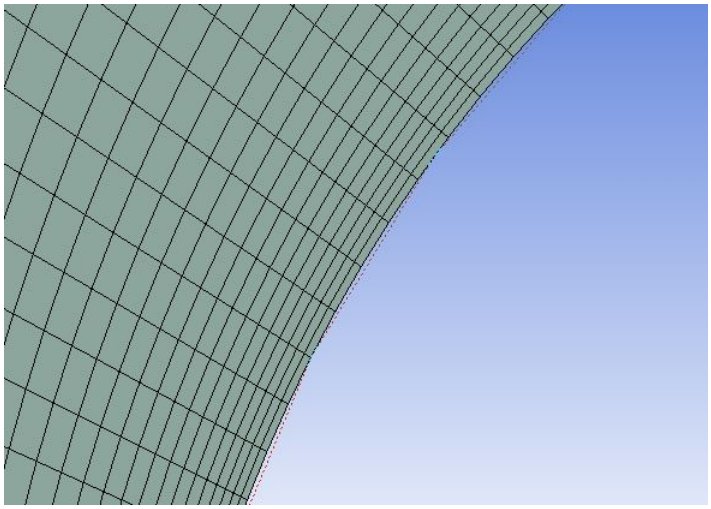

Figure 4.4: Local mesh at the surface for single cylinder.

Far-away region is meshed afterwards. The far-away region makes use of a mapped face mesh with same element size around $10h_1$. The above two dimensional mesh is extruded in the spanwise direction and the edge size is also $10h_1$. The global mesh in the side view is shown in Figure 4.5. The mesh is regular in each small block, and all the elements are hexahedron mesh.

Table 4.2 lists the mesh data in different regions. It can be found that by using this typology,

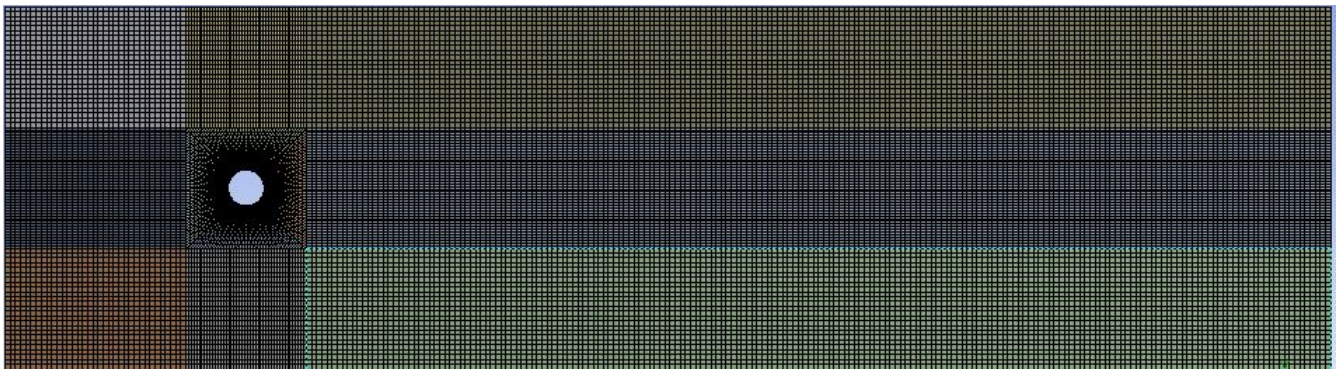

Figure 4.5: Global mesh for single cylinder.

the core region account for three-fourth of the elements. The skewness and orthogonal quality confirms that the overall quality of mesh is above level "Good", but elements in core region is a bit worse than in far-away region. This is due to the curvation of cells and the large cell length along the span.

Table 4.2: Mesh statistics for single cylinder.

Region	No. of elements	Volume	Skewness	Orthogonality
Core region	737250	9.24×10^{4} m^3	$10^{-2} \sim 0.5$	$0.71 \sim 0.99$
Far-away region	216000	1.41×10^{-2} m^3	$10^{-10} \sim 10^{-5}$	1
Total	953250	1.49×10^{-2} m^3		

The largest aspect ratio in the present case is lower than 100. At the surface of the body, this value is lower than 5 in the $X_1 Z_1$ plane.

4.3.2 Intersecting cylinders

The intersecting cylinders undoubtedly encourage the complexity of domain shape as well as the flow characteristics, especially in the region very close to the junction point. For this reason, it is unwise to repeat the same block topology like single cylinder. This is also proved by a statistics of mesh information later in this section. Then unstructured mesh is an alternative. The block topology for the domain is illustrated in Figure 4.6. The strategy is to simply vertically divide the whole domain into two main regions, which are named far-away region and transition region.

The mesh begins simultaneously in the transition region and far-away region. Similar to the single cylinder case, the special wall treatment requires a very fine cell distribution near the wall.

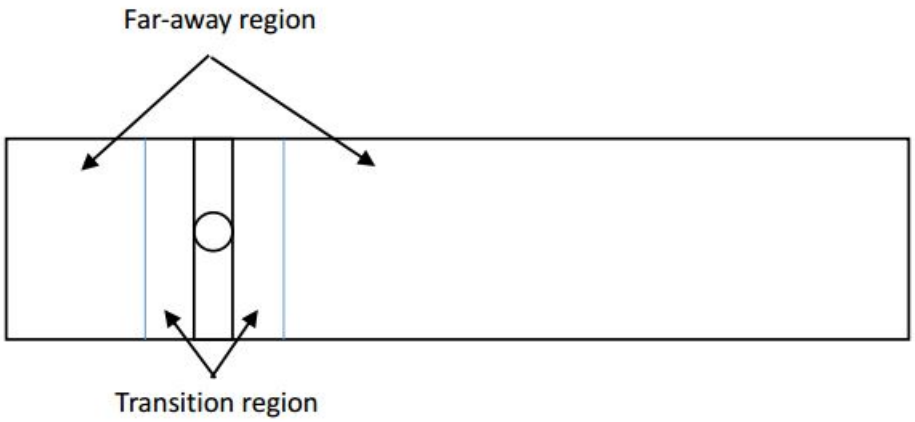

Figure 4.6: The block-typology for the whole domain in lateral view.

A thin inflation layer with then layers close to the surface is applied. These layers use structured hex mesh and the first layer thickness h_2 satisfies a y^+ value smaller than unity. Figure 4.7 shows the profile of the local mesh at the body surface. The elements are uniformly distributed along the circle. A growth rate around 1.2 is given and the thickness of the tenth layer is $10h_2$.

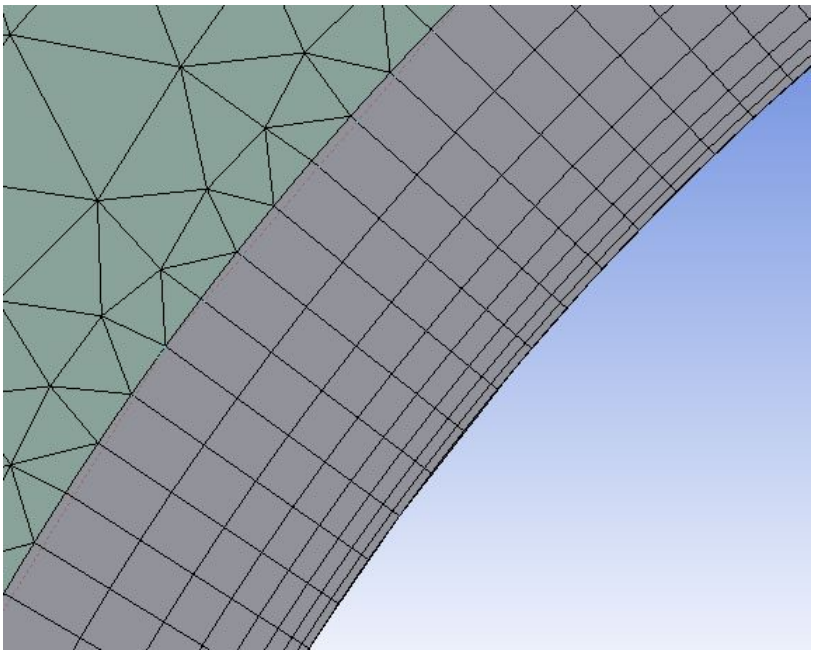

Figure 4.7: Local mesh at the surface for intersecting cylinders.

Due to the high quality of mesh in the inflation layer, the number of elements at the layer can be quite large. Therefore the span direction also uses a growth rate. Figure 4.8 shows the mesh strategy at the inflation layer. Location 1 represents the junction area while location 2

represents the place where the structure should be cut off from the 5 × 5 grid. At the junction point, the fluid motion is complex in three dimensional and the mesh element keeps an aspect ratio less than 2. At the truncation face which is $2.5D$ away from the conjunction point, the effect of interference is less important (Zdravkovich (1985)), so an aspect ratio of 15 is adopted.

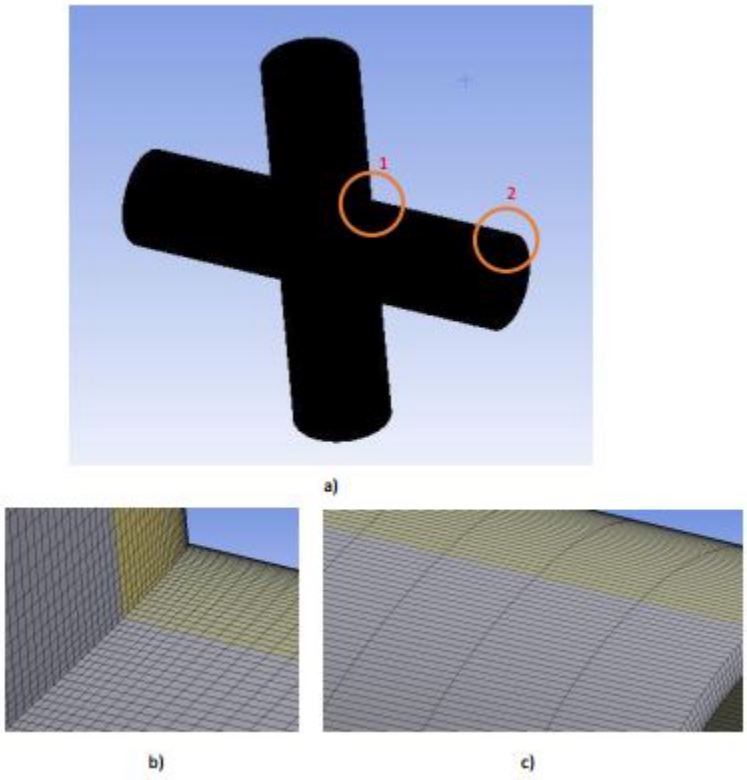

Figure 4.8: Local mesh for intersecting cylinders: a) the inflation layer; b)location 1; c)location 2.

In the far-away region, a structured hex mesh is applied. The far-away region does not need very fine mesh, so the element size here is around $70h_2$, much larger than the inflation layer. For rest volume in the transition region, unstructured mesh is applied with tetra or prism shape. The global mesh is shown in Figure 4.9.

Table 4.3 lists the mesh data in different regions. The inflation layer is the main factor that restricts the computational ability. It can be found that the volume of inflation layer only occupies about 0.3% of the total volume, but it already contains around 300000 elements, accounting for 25% of the total elements. If the inflation layer is meshed without growth rate across the span, the number of elements in the layer can reach 2 million.

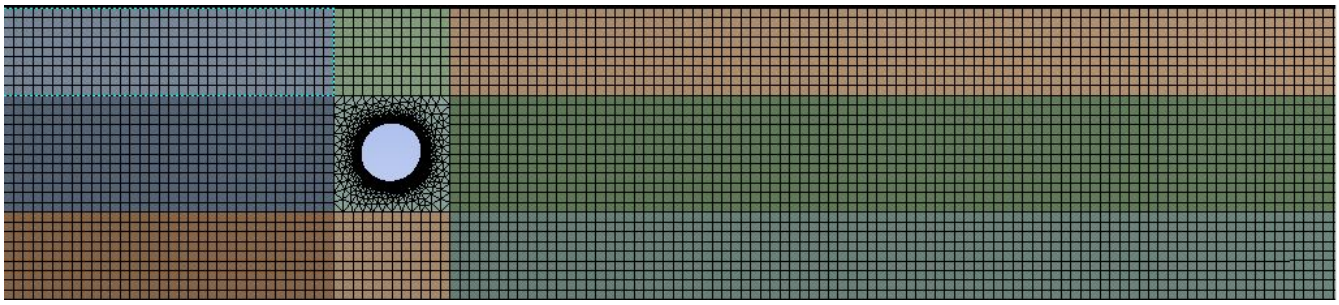

Figure 4.9: Global mesh for intersecting cylinders.

The mesh quality in the layer also influences its adjacent area in the transition region. Assuming there is a magnification ratio between inflation layer and the rest of transition region, the uniform distribution along the span will cause a total element number more than 6 million. Additionally, this number can be further larger if a fully structured mesh is made. To save time, this thesis uses the mesh listed in 4.3. The consensus here is that a fully structured mesh is of course a better choice.

Skewness and orthogonality reflect a relatively bad mesh quality in transition region. Inflation layer gets the level above "Good". In the rest of transition region, some mesh elements are even graded as "Acceptable" on skewness. It also proves the failure of mesh control by unstructured mesh.

The largest aspect ratio in the present case is also lower than 100.

Table 4.3: Mesh statistics for intersecting cylinders.

Region	No. of elements	Volume	Skewness	Orthogonality
Inflation layer	307200	$4.63 \times 10^{-5}\text{m}^3$	$10^{-8} \sim 0.54$	$0.66 \sim 0.99$
Rest of transition region	637054	$1.08 \times 10^{-3}\text{m}^3$	$10^{-4} \sim 0.82$	$0.26 \sim 0.88$
Far-away region	378300	$1.4 \times 10^{-2}\text{m}^3$	$10^{-10} \sim 10^{-7}$	1
Total	1322554	$1.5 \times 10^{-2}\text{m}^3$		

4.4 Fluent setup

Fluent setup is done in ANSYS Fluent 16.2. As the final step during the pre-processing, information of solver, turbulent model, initial and boundary conditions is specified.

4.4.1 Turbulent Model Setup

Table 4.4 lists the turbulent models. k-ω SST model and k-ϵ Realizable model are under consideration.

Table 4.4: Turbulent model setup.

Viscous model	Near wall treatment
k-ω SST	Low Re correction
k-ϵ Realizable	Enhanced wall treatment

For $k-\epsilon$ Realizable model, an enhanced wall treatment is applied in the viscous sublayer in the boundary layer.

For $k-\omega$ SST model, the resolution in the boundary layer does not rely on any special wall treatment, but a low Re correction is applied.

Two models are tested in the case of single cylinder. With a short discussion, the turbulent model is determined for intersecting cylinder case.

4.4.2 Initial conditions and boundary conditions

The overview of boundary conditions for present study is shown in Figure 4.10 and Figure 4.11. Both the two models have inlet, outlet, side boundaries and top/bottom boundaries.

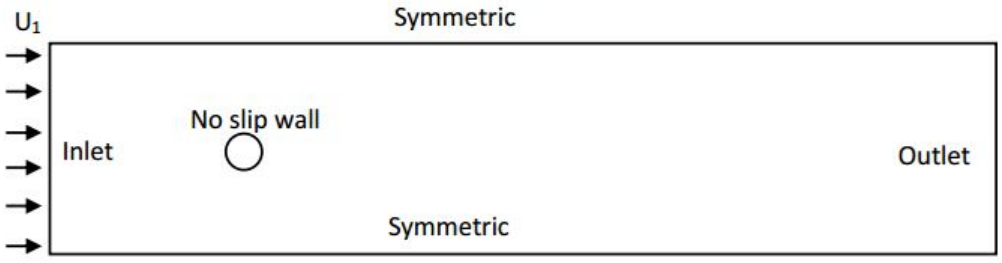

Figure 4.10: Boundary conditions for single cylinder.

A mainstream with constant value is specified at the inlet face. In the outlet boundary, the pressure is given by a pressure outlet with an averaged reference static pressure as $p_{static} = 0$. At the surface of the structure, a no slip boundary condition is specified.

For single cylinder, symmetry is applied at the top and bottom boundaries.

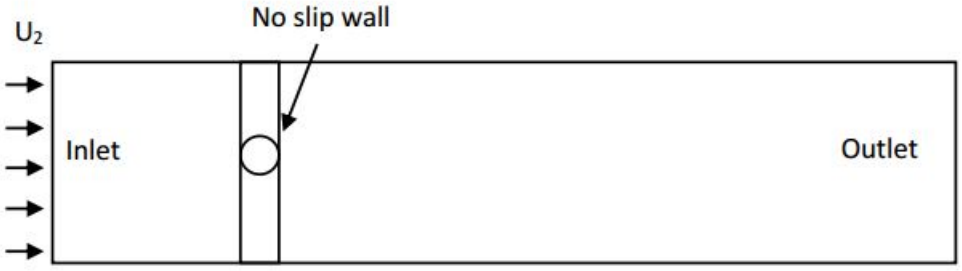

Figure 4.11: Boundary conditions for intersecting cylinders.

For the two cases, there are multiple options at the boundaries where the structure is truncated. To weaken effect from the finite spanwise length in the domain, the boundary conditions should be carefully chosen. Ma et al. (2000) set up a symmetric boundary condition by assuming zero gradient conditions at side boundary. The side boundary then become a mirror, where separation occurred at the two side of the boundary. In contrast, Tremblay et al. (2000) applied a translational periodic boundary conditions, where the cylinder was merely translated in normal direction. Two options, symmetric and periodic boundaries, are going to be tested for a single cylinder.

The information of types of boundary conditions mentioned above are concluded in Table 4.5.

Table 4.5: Boundary conditions.

Boundary conditions	Physical meaning
Velocity inlet	Specified velocity U_1=0.122 m/s, U_2=0.2 m/s
Pressure outlet	Specified static pressure P=0
No-slip wall	Zero normal and tangential velocity u_n=u_t=0
Symmetry	Zero normal velocity u_n=0 and zero tangential velocity gradient $\frac{\partial u_t}{\partial n}$=0
Translational Periodic	Same velocity profile at periodic faces $u_{face1} = u_{face2}$

4.4.3 Solver Setup

Table 4.6 summarizes the CFD settings and options in ANSYS Fluent. An unsteady and pressure based solver is used. As a routine incompressible flow problem, SIMPLE is selected as the solver. Because solver is not the major topic in the thesis, default settings are applied for interpolations. Spacial discretization is specified in the table for different turbulence models.

Table 4.6: Solver setup.

Settings	Options
Simulation type	3D, Transient
Solver	Double precision, Pressure based and Implicit
Pressure-velocity coupling	SIMPLE
Gradient	Least squares cell based
Pressure	Second order
Momentum	Second order upwind
Turbulent kinetic energy	First order upwind
Turbulent dissipation rate ($k-\epsilon$ Realizable)	First order upwind
Specific dissipation rate ($k-\omega$ SST)	First order upwind

Time step Δt is used in order to ensure a temporary Independence. From the test in the following simulation, Δt=0.002 s and the maximum CFL number less than 0.8 is satisfied.

The cases are initialized by a Full Multigrid (FMG) initialization method. FMG initialization makes use of a FAS Multigrid technology in ANSYS Fluent and helps abtain a good initial condition at very low cost. A certain number of geometric mesh level is given at first. The process begins with the coarsest level and then the level grows up for several circles until the finest level is reached (ANSYS (2015)).

Chapter 5

Result and Discussion

This chapter provides the results for the numerical simulation. The main results are stated and discussed for single cylinder, intersecting cylinders.

5.1 Case 1: Flow around single cylinder

5.1.1 Mesh convergence test

To maintain that the simulation is mesh independent solution, the total number of mesh elements should be sufficient large, and the mesh convergence test is a crucial method to ensure the mesh independence. It gives evidence how many elements are needed to display a relatively accurate result in the process of simulation. A suitable mesh arrangement is necessary so that the simulation, on the one hand remains within acceptable computational cost, and on the other hand can be trusted.

For any CFD case, the mesh convergence test should at least involve three mesh types with different mesh quality: coarse, medium and fine. The medium mesh always acts as the chosen mesh. The medium mesh should be reasonable to give more converged solution compared to the coarse mesh, and be resource-saving compared to the fine mesh.

In Table 5.1, three types of mesh are listed with different mesh divisions on each direction. The element division has an increasing tendency from coarse, medium to fine and the element number satisfies a approximated ratio of 2:3:4. The spanwise element distribution remains the

same in the three cases due to the negligible velocity component in that direction. The thickness y^+ for the first cell layer is specific in the three cases.

Table 5.1: Mesh setup for mesh convergence test.

Mesh quality	Element	y_+	N_x	N_y	N_z
Coarse	662250	1.5	220	85	30
Medium	953250	0.9	280	95	30
Fine	1495350	0.7	370	111	30

Table 5.2 illustrates the test results for case 1. In each mesh quality, hydrodynamic quantities are recorded, such as force coefficients and Strouhal number. Difference between each case are compared to validate the convergence.

Table 5.2: Hydrodynamic quantities from mesh convergence test.

Mesh quality	$\overline{C_D}$	C_{Lrms}	S_t
Coarse	1.22	0.64	0.22
Medium	1.18	0.60	0.22
Fine	1.17	0.58	0.22

The data is later plotted as Figure 5.1. In Figure 5.1, coarse, medium and fine mesh are named by 1, 2 and 3. Hydrodynamic quantities from fine mesh are set as 1, while the data from the rest two cases are expressed as the percentage of that from the fine mesh in percentage. The three mesh types give the same Strouhal number, which is to say the same vortex shedding period. The values of $\overline{C_D}$ and C_{Lrms} are very close and decline as the mesh quality increases. The results from coarse mesh changes much compared to the other two mesh qualities. One can conclude that the mesh is better converged as the mesh becomes finer and medium case is chosen as the mesh type for the following studies.

5.1.2 Parameter analysis

During the pre processing in ANSYS work, some specific conditions are not determined, such as turbulent models. In this section, a parameter analyisis is investigated to understand the effects of these parameters.

Table 5.3 lists six identical cases with specific turbulent models, dimensions of the problem, the boundary conditions at the side of the domain. Force coefficients and Strouhal number

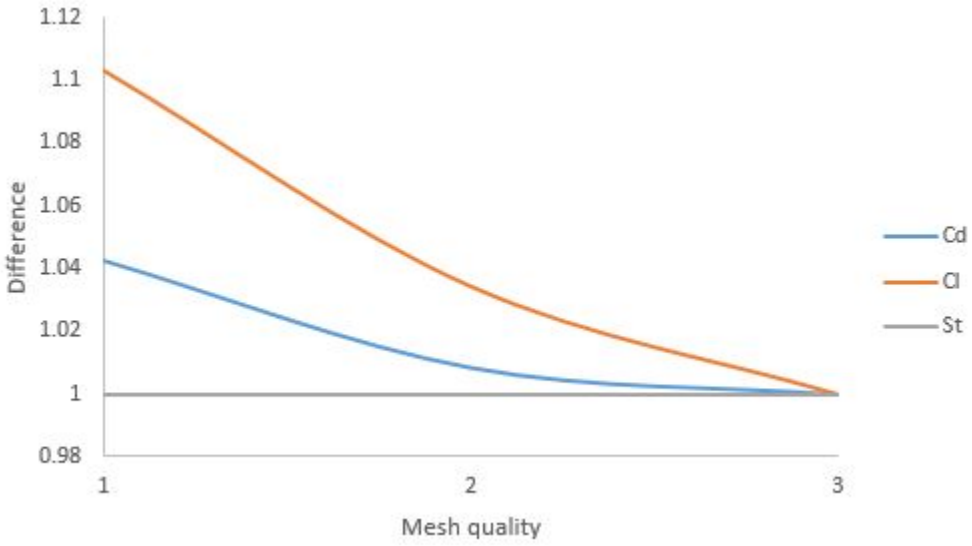

Figure 5.1: Variation of hydrodynamic quantities from mesh convergence test.

from the fluid motion are the criterion for different settings.

Table 5.3: Cases for parameter study.

Case No.	Turbulent model	Dimension	Side boundary conditions
Case 1.1	k-ω SST	2D	-
Case 1.2	k-ϵ Realizable	2D	-
Case 1.3	k-ω SST	3D	Symmetric
Case 1.4	k-ϵ Realizable	3D	Symmetric
Case 1.5	k-ω SST	3D	Periodic
Case 1.6	k-ϵ Realizable	3D	Periodic

The cases, from case 1.3 to case 1.6, are meshed by the medium mesh quality from the mesh convergence test. Case 1.1 and case 1.2 have a two dimensional domain, but are given the same geometry and mesh in the 2D profile.

Table 5.4 compares the variation of hydrodynamic quantities from 2D and 3D cases. Case 1,1 and case 1.2, in general give an over prediction of force coefficients and St. C_D, C_L for 2D are at least 50% more than 3D. St is also larger than 3D case. Two 2D cases are in consistent with the 2D RANS model by Young and Ooi (2007). The reason for the huge difference can be referred to the variation of fluid motion along the spanwise direction. At the present Reynolds number, the fluid motion already becomes three dimensional. One has found that the 2D RANS is not able to reproduce circular cylinder wake, and 3D is necessary to simulate such complex

flow (Shao and Zhang (2006)). Hence, One can conclude that 2D simulation cannot reflect the real flow characteristic.

Table 5.4: Hydrodynamic quantities from case 1.1 and case 1.4.

Case No.	C_D	C_L	St
Case 1.1	1.66	1.18	0.24
Case 1.2	1.63	1.14	0.24
Case 1.3	1.18	0.60	0.22
Case 1.4	0.87	0.21	0.22
2D RANS	1.59	1.17	0.24

Table 5.5 shows the data from different turbulent methods and boundary conditions. The reference data from published studies contains several numerical approaches at the same Reynolds number. The 3D RANS and LES results are from Young and Ooi (2007). Experimental measurement is from a PIV lab test by Lourenco and Shih (1994).

Table 5.5: Hydrodynamic quantities from case 1.3 to case 1.6.

Case No.	$\overline{C_D}$	C_{Lrms}	S_t
Case 1.3	1.18	0.60	0.22
Case 1.4	0.87	0.21	0.22
Case 1.5	1.18	0.64	0.22
Case 1.6	0.87	0.21	0.22
3D RANS	1.32	0.70	0.22
LES	1.03	0.18	0.21
Experiment	0.99	-	0.22

The PIV experiment is a general indicator of the correct solutions. It shows that the mean drag coefficient is about 0.99 and the Strouhal number is about 0.22 at Reynolds number 3900.

By comparing the predicted results with the experimental data, one can find that the predictions of drag coefficient given by RANS is still poor rather than LES performed by Young and Ooi (2007), but Strouhal number is very similar in all the cases. This shows that using a three dimensional RANS model results in only minor improvement over the two dimensional RANS model for the flow around a circular cylinder at a Reynolds number of 3900 (Young and Ooi (2007)).

Among the RANS cases, the 3D URANS performed by Young and Ooi (2007) makes use of a wall function and achieved a $y+>1$ at the near wall region, the drag coefficient is therefore even more deviated from the experiment measurement rather than present cases. An enhanced

wall treatment is proved to be able to improve the results. k-ϵ Realizable model in case 1.4 and case 1.6 underestimates the drag and lift force. The mean drag coefficient is 0.87 and root mean square value of lift is around 0.21. Another phenomenon that may be related to this lower values in k-ϵ model is the failure to reproduce the streamwise Reynolds stress (Shao and Zhang (2006)), which increase the pressure on the back side of cylinder in consequence. The rest cases, case 1.3 and case 1.5, use k-ω SST model. They achieve higher results than the experiment, and also more close to the LES results in comparison to k-ϵ model.

One can also conclude that boundary conditions have little effect on the simulation results. This is referred from a control group of case 1.3 and case 1.5 or case 1.4 and case 1.6, where the hydrodynamic quantities are almost the same in each group.

The above tables can roughly indicate the better choice in the simulation is:

- Three dimensional
- $k-\omega$ SST turbulent model

Periodic boundary conditions and symmetric boundary conditions are similar, for the next section we pick symmetric boundary conditions.

Figure 5.2 are the contours of instantaneous streamwise velocity u when the wake is fully developed at t=25 s. The plane locates at Y_1=0. Here one can observe that the vortex street develops after detachment from the cylinder and diverges after three or four cycles due to loss of energy.

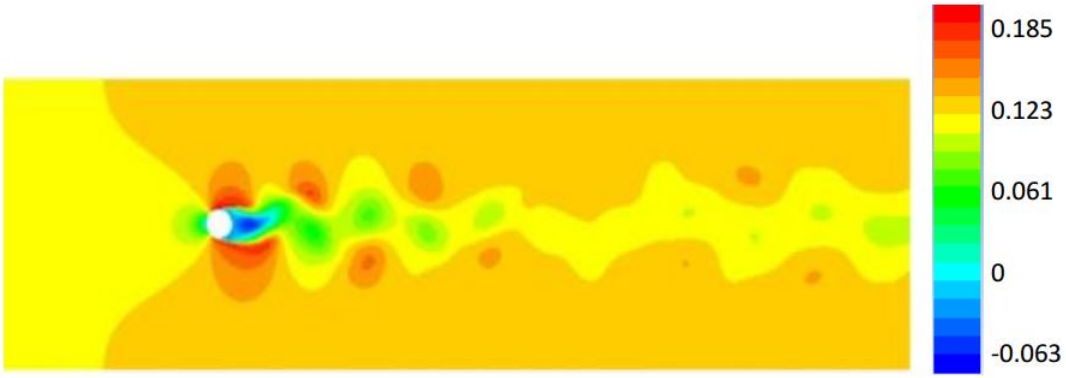

Figure 5.2: Contour of streamwise velocity [m/s].

Figure 5.3 gives the time history of drag an lift coefficient in about 15 vortex cycles. The time

scale is a non dimensional parameter $\frac{tU_1}{D}$. During this time range, the drag and lift coefficients are in stable status and oscillate around nearly constant values. From the figure, it can be observed that $\overline{C_D}$=1.18 and the maximum of lift coefficient is around 0.8. The estimation of lift period $\frac{TU_1}{D}$ is around 4.5, corresponding to the Strouhal number St=0.22.

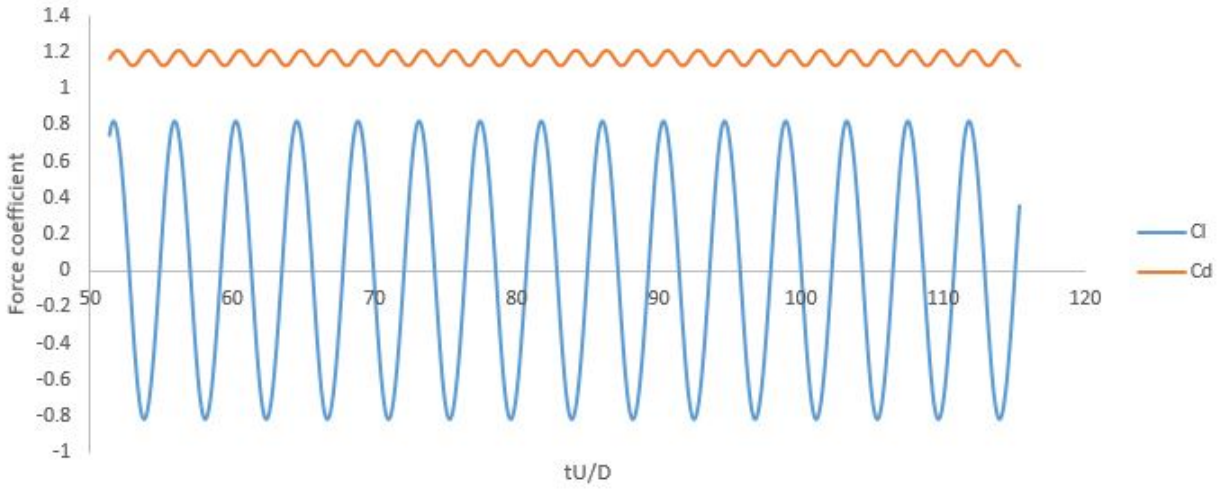

Figure 5.3: Time history of drag and lift coefficients.

5.1.3 Statistics of fluid characteristics

The velocity and pressure distribution in the fluid domain are both of great interest and can reveal the nature of the fluid motion.

The time-averaged variables can provide additional evidence to validate the results from numerical simulation. One can acquire the time averaged velocity distribution in space after sampling the data in the X_1Z_1 plane.

A normalized velocity u_n is introduced as a ratio between actual velocity u and upstream velocity U_∞ (U_1 in present case):

$$u_n = \frac{u}{U_\infty} \tag{5.1}$$

Figure 5.4 illustrates the centerline mean streamwise velocity profile. The PIV experimental data and LES result (Parnaudeau et al. (2008)) are also attached as the reference. From Figure 5.4, one can find that the present case is in a general agreement with the previous articles. All

the three curves initially experience a continuous drop within a very short distance behind the cylinder (x_1/D<2), and reach the bottom where the flow recirculation happens. After exceeding the recirculation region, the normalized velocity increases and remains stable at around 0.8 far behind the cylinder.

It can be seen that the present case fails to predict the accurate recirculation length. The recirculation length in present case is $1.7D$, while Parnaudeau et al. (2008) observed a length about $2D$. The velocity value in the wake is always a bit lower than Parnaudeau et al. (2008) in the near wake. The largest difference takes place in the recirculation region. The measured velocity at the bottom is -0.3u_n in Parnaudeau et al. (2008) and it is -0.2u_n in the present case.

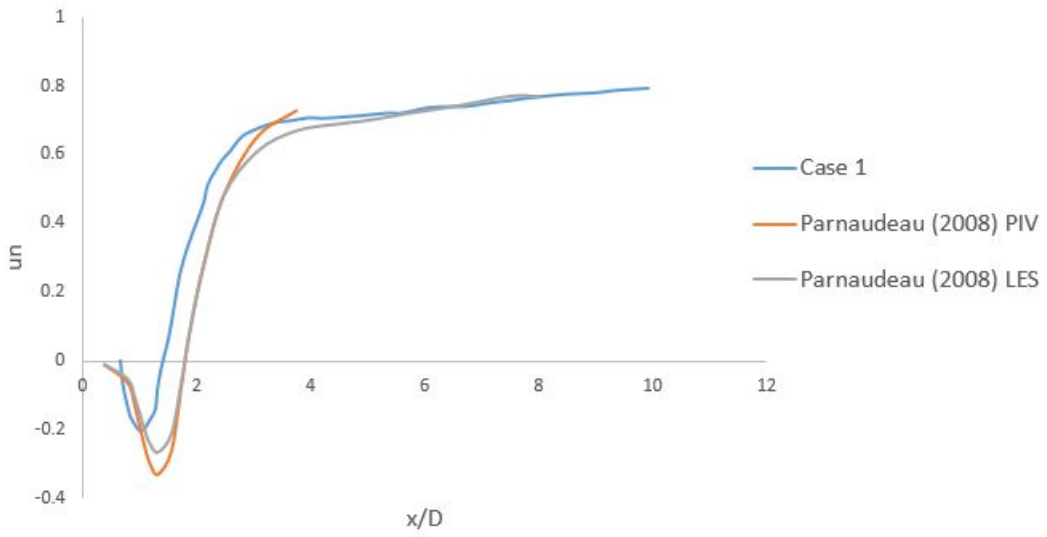

Figure 5.4: Mean streamwise velocity profile in the wake.

Figure 5.5 illustrates the vertical mean streamwise velocity profile. The profile locates at the cross section X_1/D=1.01 in comparison to the LES simulation in Parnaudeau et al. (2008). A V-shape is expected in the both LES simulation and present work, but the difference is that the velocity profile in present work is sharper.

The distribution of pressure coefficient Cp on the surface of the cylinder is depicted in Figure 5.6. Cp is plotted as a function of θ (Theta). Experiment measurement by Norberg (1987) and LES result by Breuer (1998) are attached as a reference.

For the three tests, Cp experienced a similar curve, starting with the maximum pressure, followed by a drop until θ=80 around and then kept stable at the back side of the cylinder. The

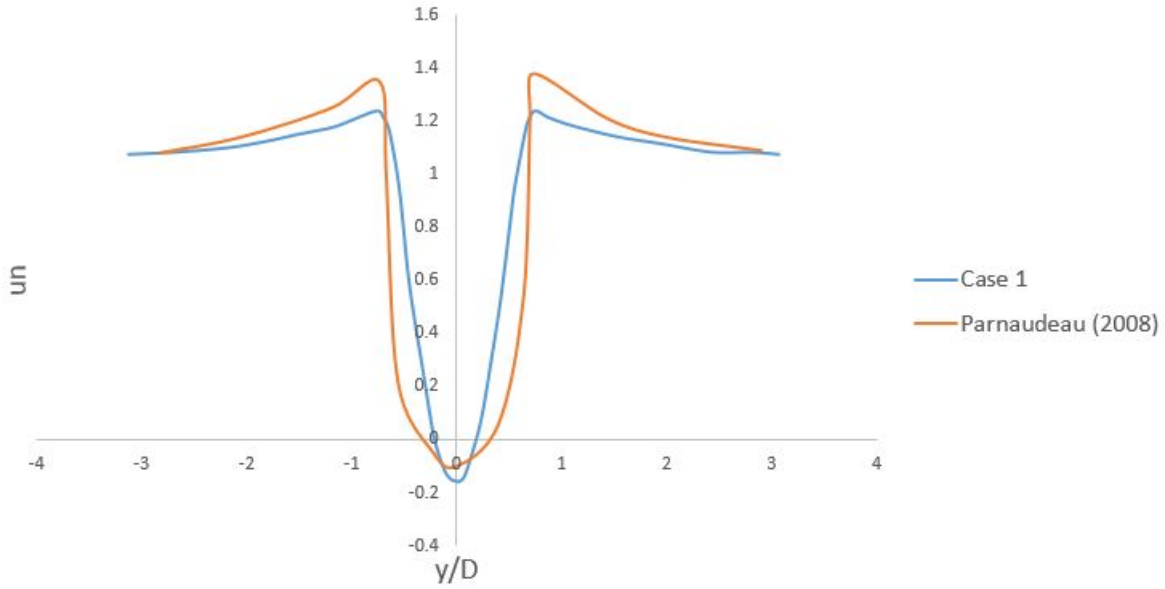

Figure 5.5: Mean streamwise velocity profile in the vertical direction.

first one-third in the curve gives very similar results while the variation appears when θ>60. The largest variation appears at the minimum Cp. Breuer (1998) and Norberg (1987) gives a Cp=-1.2 and -1.1. The present simulation with RANS abtain Cp between -1.3 and -1.4. On the back side of the cylinder, RANS overestimates Cp rather than the LES case. Considering the limitation of RANS approach, the variance between present numerical simulation and previous literature can be acceptable.

This section gives comparable results to previous literature studies at the same Reynolds number 3900. In summary, the results for single cylinders are in good agreement with the previous research. The discussion above proves that the numerical setup for the single cylinder case is able to achieve a reasonable solution at Reynolds number 3900. One can thereby concludes that ANSYS Fluent is sufficiently reliable for this kind of fluid problem. As a preliminary research, the intersecting cylinder is based on the present achievement.

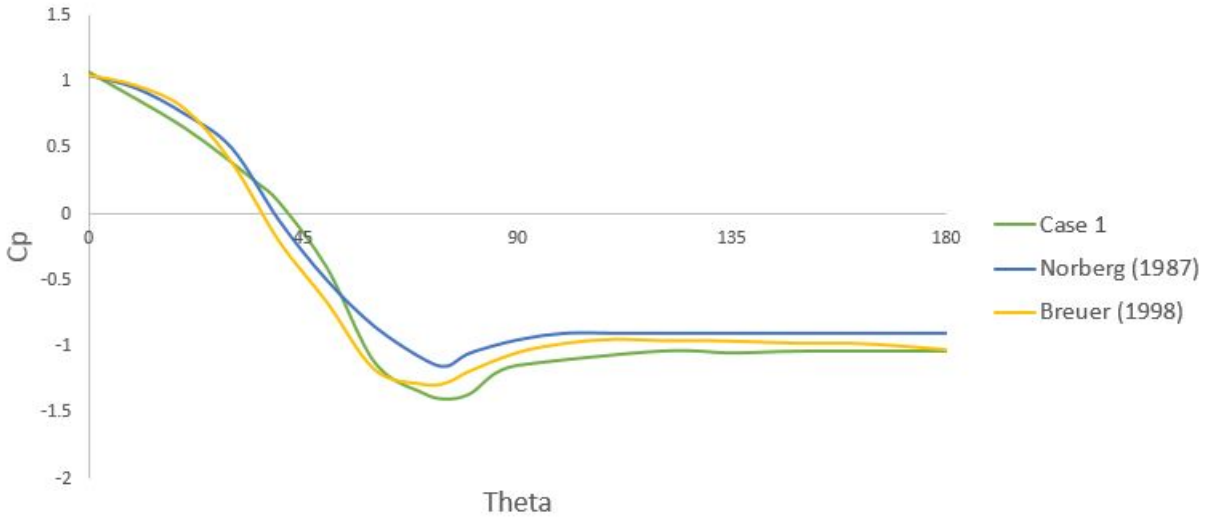

Figure 5.6: Pressure coefficient profile on the body surface.

5.2 Case 2: Flow around intersecting cylinders

5.2.1 Velocity distribution

The fluid domain is sliced at three horizontal planes, z_2=0, 30, 60 mm. Three planes with the distance represent the decreasing interference effect from the junction point on the structure.

A series of contours from Figure 5.7, Figure 5.8 and Figure 5.9 illustrate a normalized mean velocity u_n in the wake of the intersecting cylinders. The numerical results are in comparison to the 5 × 5 grid experiment.

The three figures corresponds to three X_2Y_2 planes at z_2=0, 30, 60 mm. The planes are rectangular that are defined by four points (x_2, y_2): (0.01, 0.075), (0.01, 0.075), (0.46, -0.075), (0.46, 0.075).

The increasing distance from the junction point, reflect a decreasing interference effect. The white area, where u_n=0, gives a boundary for change of sign of mean velocity. In the plane z_2=0, the vertical cylinder blocks off the fluid upstream, which reduces the fluid velocity downstream and creates a huge negative-velocity region close to the structure. As the distance z_2 goes up, the velocity becomes larger and this region becomes smaller. In the plane z_2=30mm and z_2=60mm, the maximum normalized value in the wake is more than 1.5 and 2. In the plane z_2=60mm, the contour becomes similar to a single cylinder case.

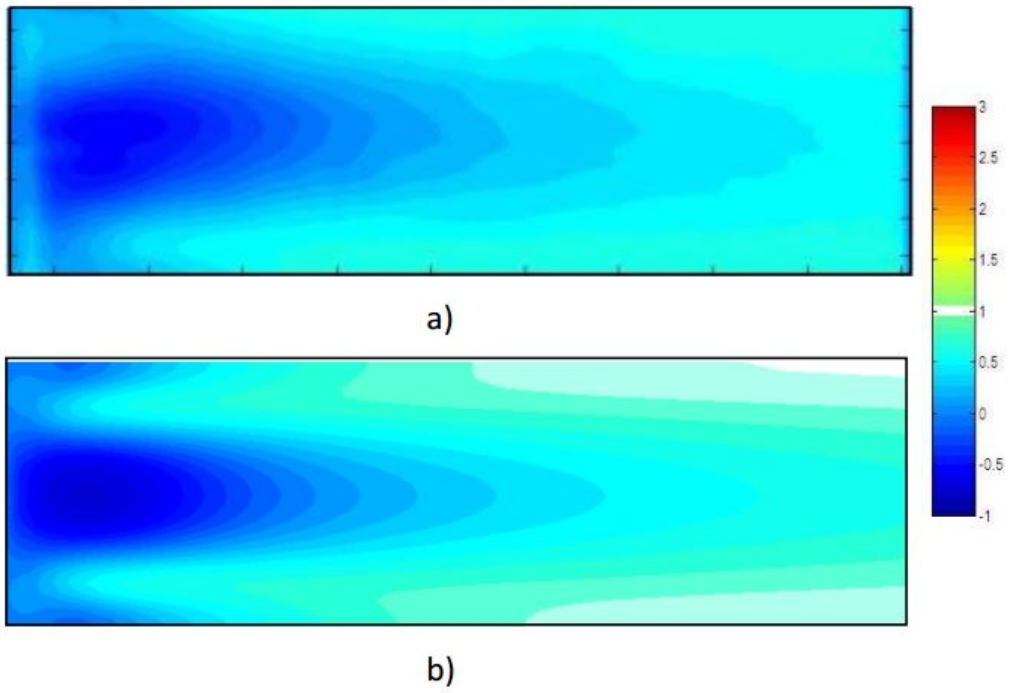

Figure 5.7: Contour of normalized velocity at z_2=0 from: a) 5 × 5 grid (Muthanna et al. (2008)); b) present case.

From the figures, the simulation can reflect the variation of velocity as z_2 changes. But it gives a larger normalized velocity than the experiment everywhere in the wake. This difference becomes more obvious as z_2 increases. Among the three positions, simulation at z_2=0 is more close to the experiment. An explanation may be that the boundary conditions in the simulation fails to model the presence of its neighbour cross-cylinder.

Muthanna et al. (2008) also provides contour from experiment for a single cruciform cylinder. This structure has the same cylinder diameter with the 5 × 5 grid, but a longer span. The numerical results of the normalized velocity are then compared to the measurement for this single cruciform cylinder. Figure 5.10 and Figure 5.11 are the contours of X_2Y_2 planes at z_2=30, 60mm. The planes remain the same size with Figure 5.7 (0.01<x_2<0.46, -0.075<y_2<0.075).

At z_2=30mm, the contour for single cruciform cylinder and 5 × 5 grid is similar. But for further place, z_2=60mm, the contour for single cruciform cylinder is more close to the simulation. The negative velocity only appears in a very thin region, just behind the structure. For the 5 × 5 grid, the interference effects result in a reduction of velocity. The white area tends to bias towards the side from Figure 5.9 to Figure 5.11.

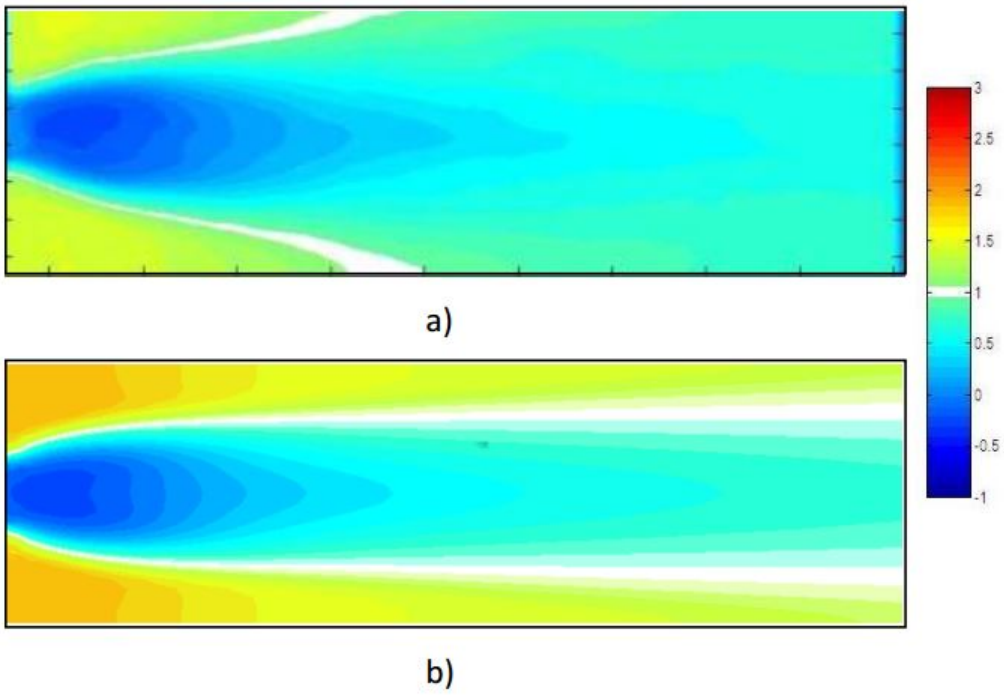

Figure 5.8: Contour of normalized velocity at z_2=30mm from: a) 5 × 5 grid (Muthanna et al. (2008)); b) present case.

Figure 5.12 illustrates u_n along the centerline for the three different X_2Y_2 planes. The curve of normalized mean velocity in case 1 is placed together. From the figure, the curve for z_2=60mm is the one close to the curve from case 1, especially when x/D>6. In the near wake, the recirculation length from the curve z_2=60mm is very small, only account for a diameter. It is reasonable to consider that the far-away wake behind the intersecting cylinders is no different from a single cylinder when it goes away from the junction point. The interference effect only occurs at the recirculation region.

5.2.2 Pressure distribution

The effect of interference can be also observed from the pressure distribution. Pressure coefficient Cp on the body surface is plotted as a function of angle from Figure 5.14. One can see distribution of Cp at different planes z_2=0.25D, D, 1.5D, 2D. The pressure distribution is compared with experiment done by Zdravkovich (1985).

By combining the series of four figures, the present work shows overall agreement with the experiment. Among the four figures, the common difference with Zdravkovich (1985) occurs at

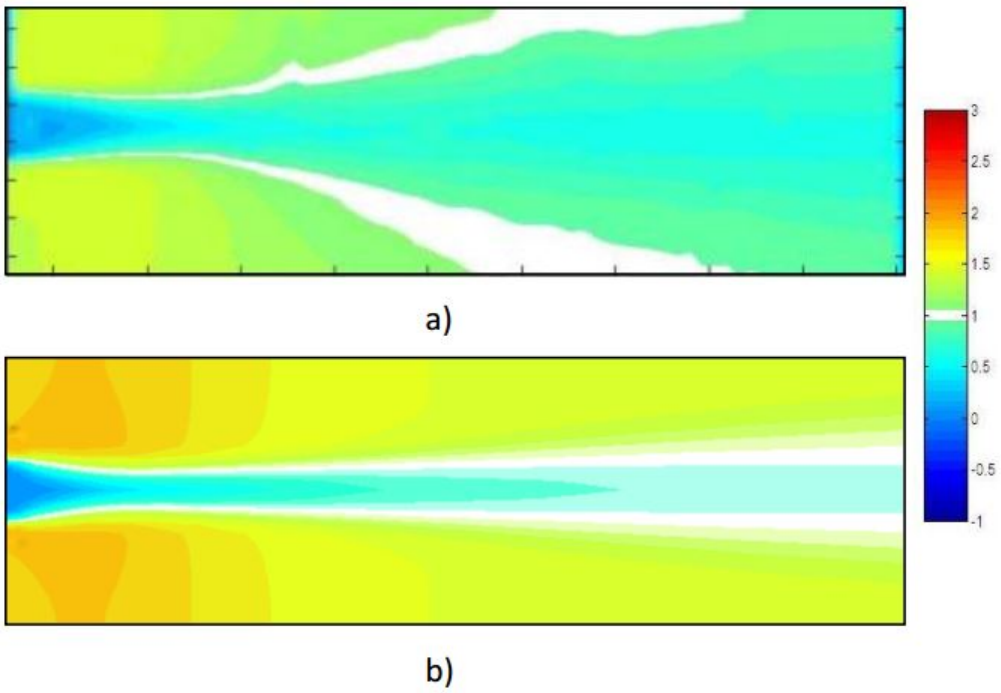

Figure 5.9: Contour of normalized velocity at z_2=60mm from: a) 5 × 5 grid (Muthanna et al. (2008)); b) present case.

the front side of the structure. The pressure coefficient at θ=0 is around 1.4 for all the planes, 40% larger than the experimental measurement. At z_2=0.25D, the curve of Cp is not complete, but the back side of the circle is almost the same. At z_2=D, 1.5D or 2D, the difference becomes more obvious.

There are two reasonable explanations. First, Zdravkovich (1985) did his experiment at a Reynolds number of 10^4. Although it is still in the subcritical regime, the fluid characteristics may be more complicated. The data is very old and causes a lost of reference value. Additionally, the mesh quality is another factor. Here, only several layers of elements are ensured as structured mesh. The transition region outsides the fine layer is filled by unstructured mesh. Mesh in this region is out of control and can affect the pressure on the body surface.

Figure 5.14 summarizes the variation of pressure coefficients from all above cases. The curves on three planes, z_2=D, 1.5D, 2D are plotted with the results z_1=D, 1.5D, 2D from case 1.

Obviously, the pressure coefficient from case 1 has a gap with case 2. Similar to the phenomenon found by Zdravkovich (1985), the effect of interference spreads even 2 diameters away

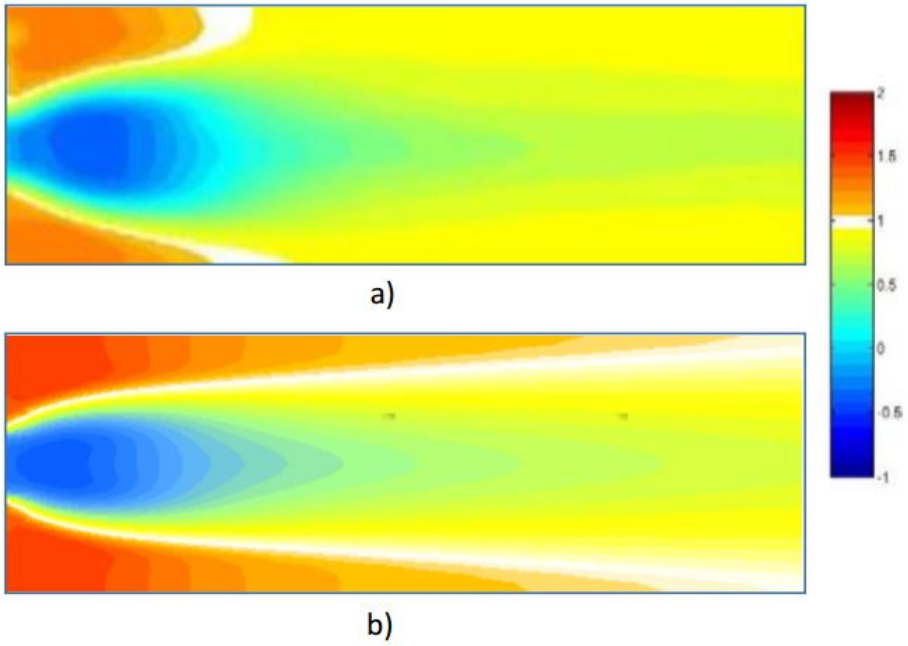

Figure 5.10: Contour of normalized velocity at z_2=30mm from: a) single cruciform (Muthanna et al. (2008)); b) present case.

from the centre of the intersection. At z_2=2D, the minimum value $C_{p,min}$ is -2.2, while the value is -1.4 for the single circular cylinder in case 1. The shape of the curves are very similar as the single cylinder.

Another phenomenon is that between 60 and 120 degree, the curves z_2=D, 1.5D, 2D intertwine with each other. This also appears from Zdravkovich (1985) and reveals that the interference is not simply decreasing as z goes larger.

From the information provided by Figure 5.14, base pressure coefficient is then plotted in Figure 5.15, as a function of z. Simulation result gives similar variation trend like that in Zdravkovich (1985). According to the measurement of Zdravkovich (1985), there should be a local minimum at z=2D. Due to the limitation of domain size, present case is unable to prove it. But it can be observed that the reduction slows down at z=2D. A local peak value is possibly located close to z=2D.

Zdravkovich (1985) inferred that the local maximum pressure is related to the distorted separation lines on the surface. Figure 5.16 sketches the flow pattern at the body surface from the top view. A plane at z_2=17mm is sliced and the plane area is equal to the projected area of the structure. The development of velocity vector on the plane is plotted in arrows. The blue line

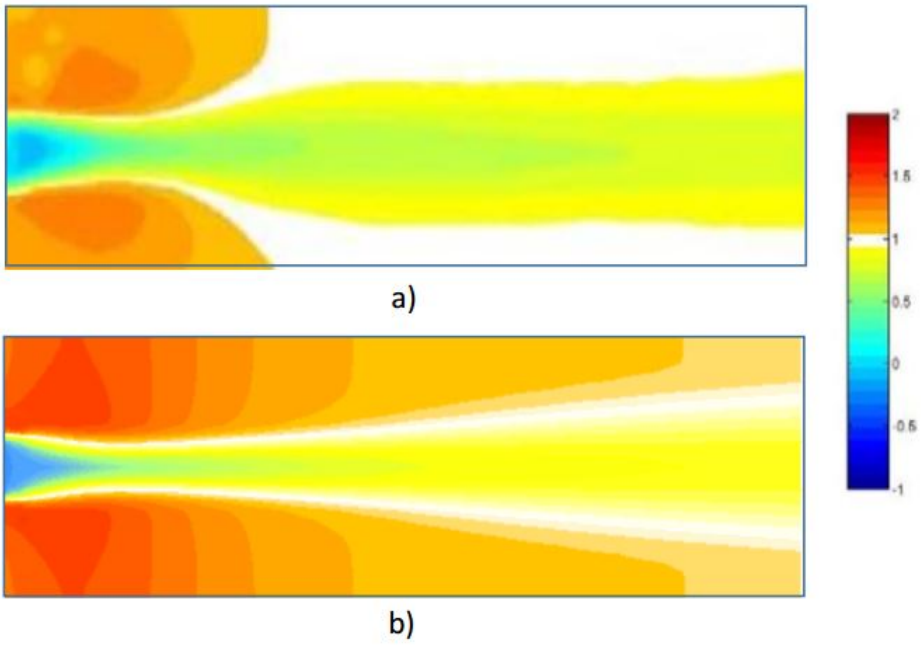

Figure 5.11: Contour of normalized velocity at z_2=60mm from: a) single cruciform (Muthanna et al. (2008)); b) present case.

in the figure roughly draws the separation lines. The region determined by the black circle confirms the presence of secondary flow and adverse pressure gradient, as seen in the photo from Zdravkovich (1985) as well. The flow can be also assumed symmetric about its axis from the figure.

Considering the information of both velocity and pressure, the simulation regarding the intersecting cylinders obtains valuable results. There exists some difference with experimental measurement. Besides the inaccuracy of the model, the lack of pressure data from Muthanna et al. (2008) is one reason. The mesh quality is another main influence factor. The solution probably reveals the important role mesh quality plays on the simulation. A completely structured mesh is worth trying if permitted.

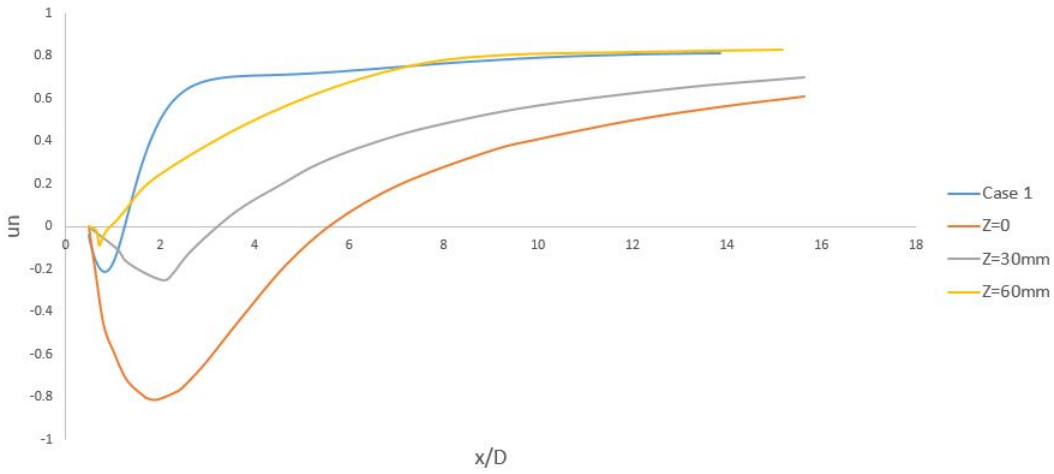

Figure 5.12: Velocity distribution along the centerline.

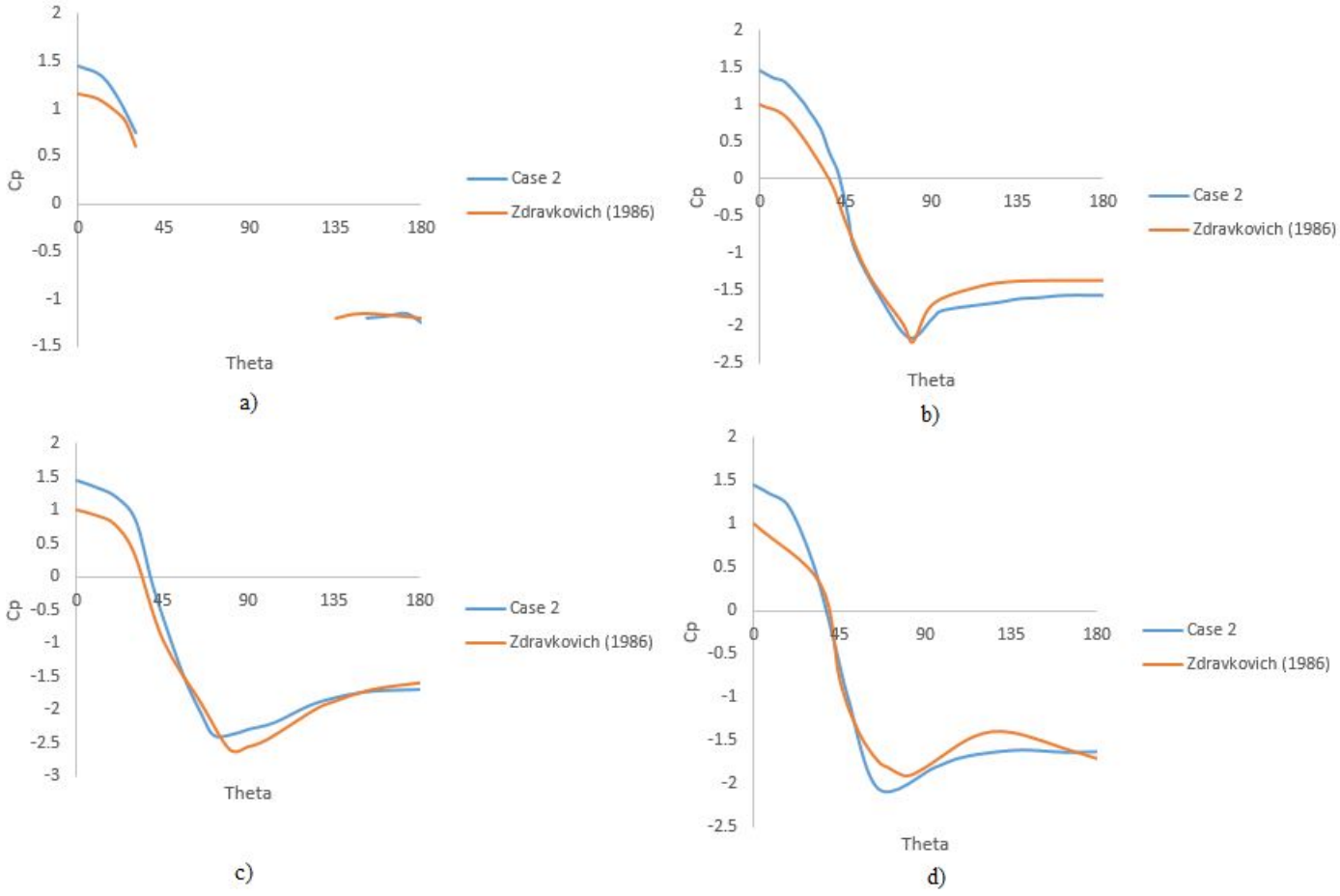

Figure 5.13: Pressure coefficient profile: a) z_2=0.25D; b) z_2=D; c) z_2=1.5D; d) z_2=2D.

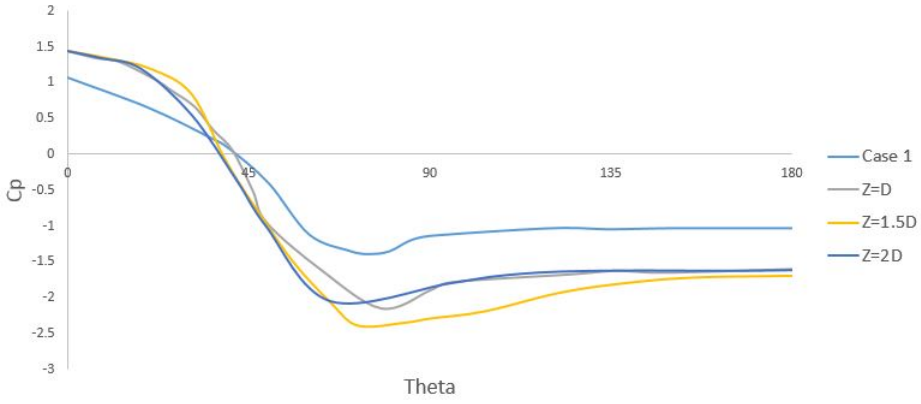

Figure 5.14: Pressure coefficient profile for different cases.

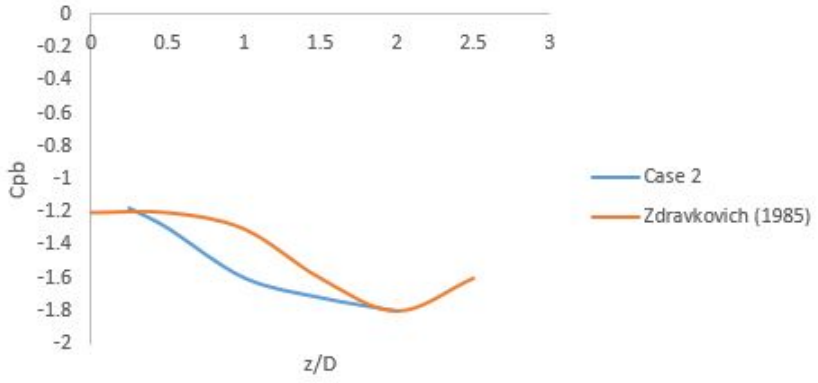

Figure 5.15: Base pressure coefficient along the span.

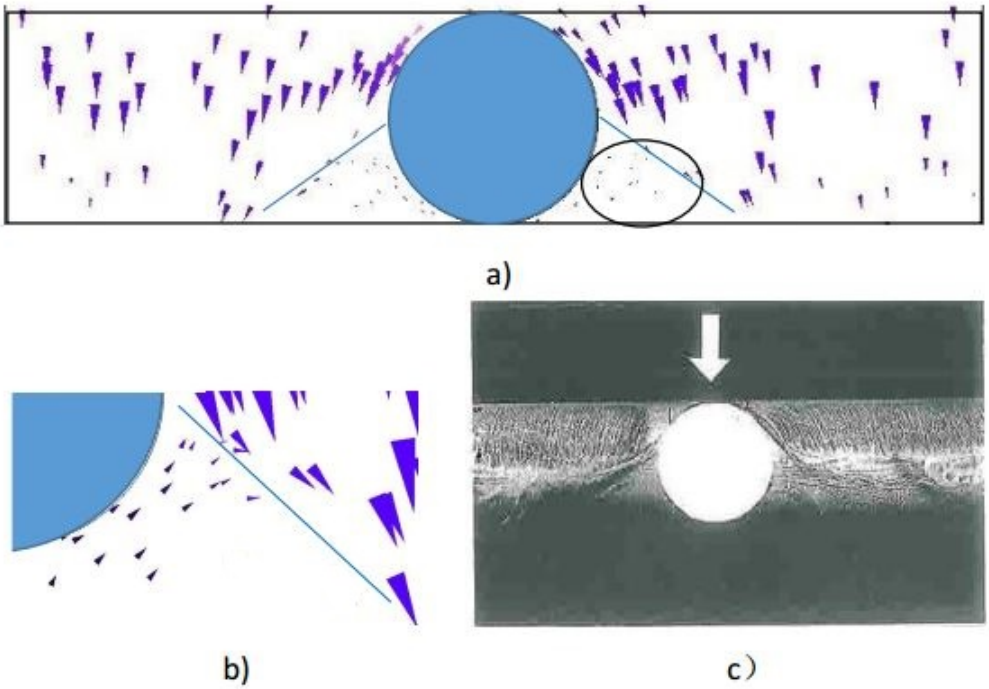

Figure 5.16: Flow pattern from top view: a) velocity vector at z_2=17mm; b) part of a); c) photo at the surface by Zdravkovich (1985).

Chapter 6

Conclusion

This thesis performed a numerical simulation of flow through a cross-cylinder structure. A RANS approach with $k-\omega$ SST model was applied. The present numerical model has proved to be a valuable tool for the computation of flow around cylindrical structures with acceptable errors.

- Case 1, flow around a three dimensional circular cylinder at Reynolds number 3900, is studied. The fluid domain is defined from a review of previous numerical simulations. A multi-block mesh typology is applied. The mesh based on this typology is later examined through a mesh convergence test. In the convergence test, three mesh cases are defined: coarse, medium and fine mesh. The cases are ensured by a small elements in the boundary layer and distinguished by different numbers of grid in each direction. The mesh quality is proved through the observation of Strouhal number, drag and lift coefficients.

  A parameter investigation for flow around circular cylinder at Reynolds number of 3900 is conducted. The effects of dimension of problem, RANS Turbulent models and boundary conditions are studied by a comparison to published articles. Velocity and pressure distribution are discussed through curves and contours. The results of pressure and velocity have small difference with the LES and experiment results, but show the same tendency. It is concluded that the ANSYS Fluent is able to perform this type of fluid problem.

- Case 2, flow around a cross-cylinder structure is implemented on a basis of case 1. The domain is determined after the PIV experiment by Muthanna et al. (2008). Part of the

domain is made of unstructured mesh to reduce the element number. Mesh convergence test is not considered due to the unstructured mesh, but several mesh metrics show an acceptable mesh quality.

The simulation is performed at Reynolds number 6400. By comparing the contours of mean streamwise velocity, the present simulation provides a little overprediction of the mean velocity in the wake. The velocity profile at the edge of the structure behaves more similar to a single cylinder case, but interference effects still exist. The mean streamwise velocity is more close to the experiment of single cruciform cylinders, rather than the 5 × 5 grid test. So a numerical simulation regarding the complete grid should be conducted in the future.

By plotting the pressure coefficients C_p and C_{pb}, pressure distribution on the body is observed. One interesting finding is that the interference on the pressure is not simply decreasing as the distance increases from the junction point.

A secondary flow pushes the mainstream flow to both sides. The adverse pressure gradient on the body surface is an important factor to cause the pressure maximum along the span. The flow pattern is possibly symmetric from the velocity vector distribution.

Chapter 7

Recommendations for Further Work

The following are some recommendation for further work.

- Due to the limitation of available resource on Vilje, case 2 uses a mesh typology combining structured and unstructured grids. Only a fine mesh close to the wall was ensured for the special wall treatment. The mesh convergence test is not given in this case because it is difficult to control the mesh quality for unstructured mesh. It is better to set up a fully structured mesh and run a new case with a complete mesh convergence test.

- Experimental measurement (Zdravkovich (1985)) shows that the interference effects on the surface of intersecting cylinders is still strong even far away from the junction point. Present study gives a growth rate in the spanwise direction. As the distance increases, the element becomes longer. A finer mesh should be implemented along the span in the future.

- For special reasons, the experimental report (Muthanna et al. (2008)) is not a complete version. In case 2, only velocity distribution are discussed with this experiment. In further work, the characteristics of pressure distribution and drag force on the surface can be studied with more detailed data.

- This thesis makes use of a pair of intersecting cylinders to model a 5×5 grid in a lab test. Better solutions can be expected if the whole net structure is modeled.

- Solver is also a topic of interest, such as LES. In case 1, RANS approach shows a relatively bad solution compared to a LES approach.

Bibliography

ANSYS, I. (2015). Ansys user guide 16.2.

Bi, C.-W., Zhao, Y.-P., Dong, G.-H., Xu, T.-J., and Gui, F.-K. (2014). Numerical simulation of the interaction between flow and flexible nets. *Journal of Fluids and Structures*, 45:180–201.

Boussinesq, J. (1877). *Essai sur la théorie des eaux courantes*. Imprimerie nationale.

Breuer, M. (1998). Large eddy simulation of the subcritical flow past a circular cylinder: numerical and modeling aspects. *International Journal for Numerical Methods in Fluids*, 28(9):1281–1302.

DeCew, J., Tsukrov, I., Risso, A., Swift, M., and Celikkol, B. (2010). Modeling of dynamic behavior of a single-point moored submersible fish cage under currents. *Aquacultural Engineering*, 43(2):38–45.

Ferziger, J. H. (2002). Peri c m., computational methods for fluid dynamics.

Fox, T. and Toy, N. (1990). Wind effects on structural intersections. *Journal of Wind Engineering and Industrial Aerodynamics*, 34(1):27–44.

Franke, J. and Frank, W. (2002). Large eddy simulation of the flow past a circular cylinder at re d= 3900. *Journal of wind engineering and industrial aerodynamics*, 90(10):1191–1206.

Gansel, L. C., Rackebrandt, S., Oppedal, F., and McClimans, T. A. (2014). Flow fields inside stocked fish cages and the near environment. *Journal of Offshore Mechanics and Arctic Engineering*, 136(3):031201.

Harendza, A., Visscher, J., Gansel, L., and Pettersen, B. (2008). Piv on inclined cylinder shaped fish cages in a current and the resulting flow field. In *ASME 2008 27th International Conference on Offshore Mechanics and Arctic Engineering*, pages 555–563. American Society of Mechanical Engineers.

Kravchenko, A. G. and Moin, P. (2000). Numerical studies of flow over a circular cylinder at re d= 3900. *Physics of fluids*, 12(2):403–417.

Lader, P., Dempster, T., Fredheim, A., and Jensen, Ø. (2008). Current induced net deformations in full-scale sea-cages for atlantic salmon (salmo salar). *Aquacultural Engineering*, 38(1):52–65.

Lader, P. F. and Enerhaug, B. (2005). Experimental investigation of forces and geometry of a net cage in uniform flow. *IEEE Journal of Oceanic Engineering*, 30(1):79–84.

Lader, P. F., Enerhaug, B., Fredheim, A., and Krokstad, J. (2003). Modelling of 3d net structures exposed to waves and current. In *3rd International Conference on Hydroelasticity in Marine Technology*, pages 19–26. Department of Engineering Science, The University of Oxford Oxford, UK.

Lader, P. F. and Fredheim, A. (2006). Dynamic properties of a flexible net sheet in waves and current—a numerical approach. *Aquacultural engineering*, 35(3):228–238.

Li, Y. Z. (2011). Large eddy simulation of flow around a cylinder at re= 3900 using a cfd code. In *Applied Mechanics and Materials*, volume 94, pages 1707–1710. Trans Tech Publ.

Lourenco, L. and Shih, C. (1994). Characteristics of the plane turbulent near wake of a circular cylinder, a particle image velocimetry study. *Technical report TF-62*.

Ma, X., Karamanos, G.-S., and Karniadakis, G. (2000). Dynamics and low-dimensionality of a turbulent near wake. *Journal of Fluid Mechanics*, 410:29–65.

Menter, F. R. (1993). Zonal two equation k-turbulence models for aerodynamic flows. *AIAA paper*, 2906:1993.

Muthanna, C., Visscher, J., and Pettersen, B. (2008). Investigating fluid flow phenomena behind intersecting and tapered cylinders using submerged stereoscopic piv. In *14th Int Symp on Applications of Laser Techniques to Fluid Mechanics Lisbon, Portugal*, pages 07–10.

Norberg, C. (1987). Effects of reynolds number and a low-intensity freestream turbulence on the flow around a circular cylinder. *Chalmers University, Goteborg, Sweden, Technological Publications*, 87(2).

Osaka, H., Nakamura, I., Yamada, H., KUwATA, Y., and Kageyama, Y. (1983). The structure of a turbulent wake behind a cruciform circular cylinder: 1st report, the mean velocity field. *Bulletin of JSME*, 26(213):356–363.

Palkin, E., Mullyadzhanov, R., and Hanjalic, K. Urans and les of a flow over a cylinder at re= 3900.

Parnaudeau, P., Carlier, J., Heitz, D., and Lamballais, E. (2008). Experimental and numerical studies of the flow over a circular cylinder at reynolds number 3900. *Physics of Fluids (1994-present)*, 20(8):085101.

Patursson, Ø., Swift, M. R., Baldwin, K., Tsukrov, I., and Simonsen, K. (2006). Modeling flow through and around a net panel using computational fluid dynamics. In *OCEANS 2006*, pages 1–5. IEEE.

Patursson, Ø., Swift, M. R., Tsukrov, I., Simonsen, K., Baldwin, K., Fredriksson, D. W., and Celikkol, B. (2010). Development of a porous media model with application to flow through and around a net panel. *Ocean Engineering*, 37(2):314–324.

Shao, J. and Zhang, C. (2006). Numerical analysis of the flow around a circular cylinder using rans and les. *International Journal of Computational Fluid Dynamics*, 20(5):301–307.

Shih, T.-H., Liou, W. W., Shabbir, A., Yang, Z., and Zhu, J. (1995). A new k- eddy viscosity model for high reynolds number turbulent flows. *Computers & Fluids*, 24(3):227–238.

Sumer, B. M. and Fredsøe, J. (1997). *Hydrodynamics around cylindrical structures*, volume 12. World Scientific.

Tennekes, H. and Lumley, J. L. (1972). *A first course in turbulence*. MIT press.

Tremblay, F., Manhart, M., and Friedrich, R. (2000). Dns of flow around a circular cylinder at a cubcritical reynolds number with cartesian grids. *Advances in Turbulence VIII*, pages 659–662.

Young, M. and Ooi, A. (2007). Comparative assessment of les and urans for flow over a cylinder at a reynolds number of 3900. In *16th Australasian Fluid Mechanics Conference (AFMC)*, pages 1063–1070. School of Engineering, The University of Queensland.

Zdravkovich, M. (1985). Flow around two intersecting circular cylinders. *Journal of fluids engineering*, 107(4):507–511.

Zhan, J., Jia, X., Li, Y., Sun, M., Guo, G., and Hu, Y. (2006). Analytical and experimental investigation of drag on nets of fish cages. *Aquacultural engineering*, 35(1):91–101.

Zhao, Y.-P., Bi, C.-W., Dong, G.-H., Gui, F.-K., Cui, Y., Guan, C.-T., and Xu, T.-J. (2013). Numerical simulation of the flow around fishing plane nets using the porous media model. *Ocean Engineering*, 62:25–37.

Zhao, Y.-p., LI, Y.-c., GUI, F.-k., and DONG, G.-h. (2007). Numerical simulation of the effects of weight system on the hydrodynamic behavior of 3-d net of gravity cage in current. *Journal of Hydrodynamics, Ser. B*, 19(4):442–452.